A first step towards the modeling of intervertebral disc tissue reconstruction
– Master Thesis Report –

Violette Brulliard

May 15, 2010

Master of Science in Computational Mechanics, 2008-2010

Supervisors: Steven Le Corre, Erwan Verron

Contents

List of Figures

List of Tables

1 Introduction

Intervertebral discs provide flexibility of the spine and transmit and distribute large loads through the spine. To carry out these tasks the intervertebral discs have a particularly complex structure consisting of a gelatinous nucleus pulposus and the annulus fibrosus. However, many people show degenerative changes in the intervertebral discs due to aging or pathological process. These changes affect the composition and structure of the intervertebral discs, and their mechanical functions too. Back pain is often a clinical consequence of disc degeneration.

The full understanding of the role of each one of the components of the intervertebral disc in the mechanical response of the spine, as well as the mechanism of disc degeneration is of major interest. Indeed, it would help proposing alternatives in order to relieve patients who show back pain related to degenerated discs. Several analytic and finite element models have already been used to predict the behavior of the IVD, to investigate the process of disc degeneration, or to understand the complex exchange mechanisms that occur within the IVD.

The present study aims at trying to better understand the individual role of the nucleus pulposus and the annulus fibrosus using a simplified geometry and constitutive framework compared to the reality.

The first chapter presents the background of this study with a description of the IVD and the objectives of the work. The second chapter is an overview of some models of IVDs found in the literature. The third chapter sets the basics of our intervertebral disc model: choice of non-linear incompressible viscoelasticity, and its numerical implementation using Matlab and the finite element software COMSOL Multiphysics. In chapter five, some results of the corresponding calculations are presented. Finally, chapter six gives a summary of the study and proposes a discussion about the choices that have been made and future work.

2 Background

This chapter is divided into two main parts. The first one provides an overview of the intervertebral disc characteristics. A description of a healthy adult intervertebral disc is made. The emphasis is on the main components of the intervertebral disc which are described in terms of structure, composition and mechanical functions. The phenomenon of disc degeneration is then tackled: the changes in structure and composition of a degenerated disc compared to a healthy disc are presented, as well as the possible causes of degeneration. Eventually, some solutions of disc reconstruction are presented. The second part of the chapter deals with the objectives of the present study.

2.1 Motivation

2.1.1 The intervertebral disc

The intervertebral disc (IVD) is the soft tissue present between adjacent vertebral bodies. There are a total of 23 discs in the entire length of the spine between the cervical, thoracic and lumbar vertebrae. When the height of all the discs is considered, they represent approximately 25% of the total height of the vertebral column. Two adjacent vertebrae and their intervening intervertebral disc (Figure 1) are termed a functional spinal unit (FSU) or motion segment.

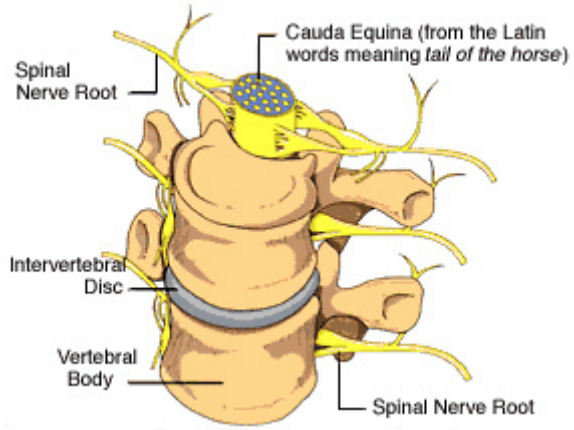

Figure 1: Motion segment (two adjacent vertebrae and their intervening intervertebral disc)

The intervertebral disc is composed of three main components: the nucleus pulposus, annulus fibrosus, and the cartilaginous endplate. The centrally located nucleus pulposus (NP) is surrounded by the annulus fibrosus (AF) made of concen-

trically arranged collagen fibrils (Figure 2). This structure, in turn, is sandwiched between two cartilaginous endplates. Thus, the disc is attached to the vertebral body above and below [24]. All regions of the disc consist mainly of an extracellular matrix of collagen fibrils inflated by water [26], but they differ significantly in structure and function.

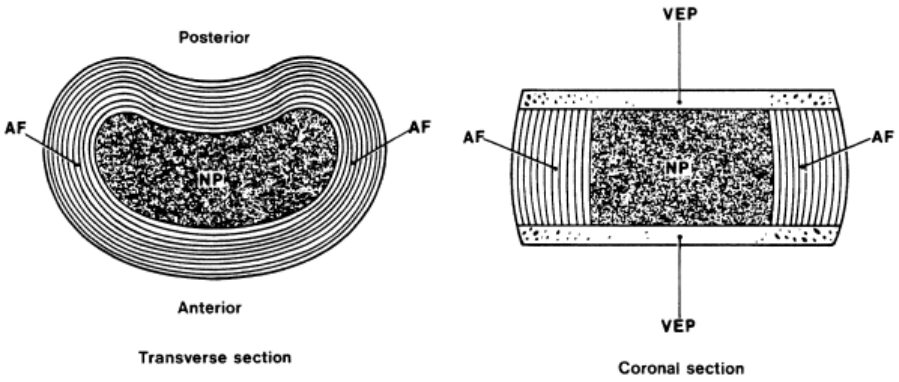

Figure 2: Anatomy of the intervertebral disc (NP - Nucleus pulposus; AF - Annulus Fibrosus; VEP - Vertebral Endplate)

The cartilaginous endplates At the boundary between the vertebral body and the IVD lies a thin layer (approximately 1 mm) of cartilage, comprising the cartilaginous endplate. Resembling articular cartilage, the cartilaginous endplate is comprised of 70-80% water and 7% of its dry weight is proteoglycan[1]. The cartilaginous endplate varies in composition depending on radial position with an increase in collagen content and subsequent decrease in proteoglycan and water content as the outer edge is approached. Early in life, the endplates are highly vascularized, but the degree of vascularity decreases dramatically over the course of the first year, and there are essentially no blood vessels present in the third decade.

The nucleus pulposus (NP) The soft, pulpy NP is located at the center of the IVD. It has a gelatinous, mucous-like consistency, with a milky-white appearance, often varying between opacity and translucence from one specimen to another [2]. A young and healthy NP is composed primarily of water (80%), and its dry weight is composed of 25-60% proteoglycan, 10-20% collagen, and other minor constituents.

The NP is believed to support compressive or eccentric loads on the vertebral body through fluid pressurization. Essentially, pressure resulting from an applied

[1]Proteoglycans are glycoproteins that are heavily glycosylated. They have a core protein with one or more covalently attached glycosaminoglycan (GAG) chain(s). The chains are long, linear carbohydrate polymers that are negatively charged under physiological conditions.

load presses outward on the surfaces surrounding the NP, causing the AF and the cartilaginous endplates to contain this pressure.

The annulus fibrosus (AF) The annulus fibrosus is composed of a series of 15-25 concentric layers (or lamellae) of collagen fibers. Within each lamella, the fibers lies parallel and their orientation varies, alternating at approximately $\pm 30°$ to the transverse plane of the disc [15] as shown in Figure 3. The annulus fibrosus is composed primarily of water (65-80%), and highly organized collagen. The dry weight of the outer AF is about 75-90% collagen and 10% proteoglycan while the inner AF is about 40-75% collagen and 20-30% proteoglycan.

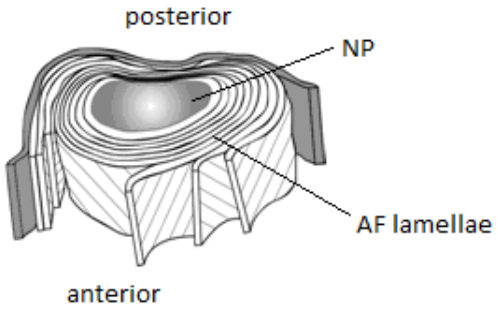

Figure 3: Annulus fibrosus lamellar structure

The collagen bundles are connected with those of the vertebral bodies, the surrounding ligaments and cartilaginous endplates, thereby securing the disc to adjacent structures. The collagen network of the annulus thus forms a reinforced structure, resisting tension. The lamellae are loosely interconnected and can move independently and slip past each other. Thus, although the collagen fibrils themselves are virtually inextensible, the whole structure is highly deformable [26]. The outermost layers of the annulus tend to be more dense and resistant to tensile forces. These layers are firmly attached to the endplates and the vertebral bodies and are reinforced by the posterior and anterior longitudinal ligaments. The areas between the lamellae are filled with elastin, which may allow the disc to return to its original position following flexion or extension [24].

2.1.2 Degeneration of the intervertebral disc

Primary degeneration of the IVD is a type of degeneration that occurs as a natural part of the aging process and is a common occurrence among all biological tissues. As age increases, the composition of the disc changes. Notably, water and proteoglycan content decreases in the NP. At birth, the hydration of the NP may be as

high as 90%, while it decreases to near 70% in adults. The proteoglycan content also decreases from 60% at birth (dry weight) to below 20% beyond middle age [2]. Macroscopically, the structural characteristics of age-related disc degeneration can be observed. The disc, which used to be white, becomes increasingly discoloured with accumulation of brown and yellow pigments as illustrated in Figure 4. The boundary between the NP and the AF becomes blurred as the NP loses hydration, and becomes more fibrocartilaginous. The NP becomes more desiccated until eventually it loses integrity and clefts appear. Cracks develop and grow in the annulus, and the lamellae become less organized. Thickness irregularity and calcification of the cartilaginous endplates have also been noted as age increases.

There are, in addition, some pathological changes (known as disc degeneration) that may affect the IVD. They occur at an accelerated rate and possibly on a larger scale than the changes occurring for age-related degeneration. Those changes include a huge loss in disc hydration, a loss of disc height, a bulge of the annulus beyond the disc space, defects and sclerosis of the endplates, and osteophytes at the vertebral apophyses.

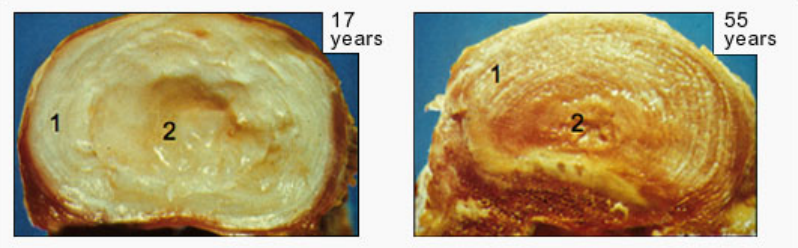

Figure 4: Comparison of the aspect of a young healthy IVD (left) and a degenerated IVD with loss of water content (right) (1 - AF; 2 - NP)

Consequent clinical problems, such as disc herniation, can result from IVD degeneration. Disc herniation occurs when the NP is forced partially or fully through a rupture in the AF or the cartilaginous endplate, and may become painful particularly when the herniated IVD material intersects the spinal cord (Figure 5).

The causes of disc degeneration are not well identified. However, several environment factors have been suspected of initiating degenerative changes in the disc: mechanical overload, excessive vibration exposure, immobility, poor posture, and chemical influences such as smoking and alcohol. Genetic factors may also cause disc degeneration.

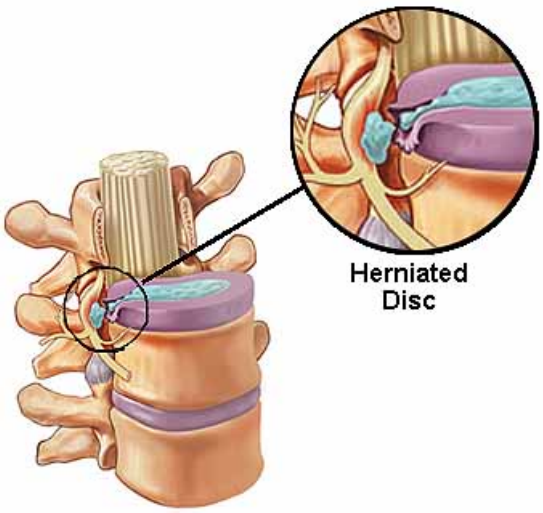

Figure 5: Herniated disc

2.1.3 Reconstruction

Low back pain is widely recognized as one of the leading causes of disability afflicting the population resulting in activity limitation and health care cost [3]. A number of studies have shown strong correlation between disc degeneration and back pain. Since, following disc disruption, discs have a very limited capacity to heal or to restore their structural activity, medical treatment have to be considered. For most people who do not have evidence of nerve root compression with muscle weakness, the first line of therapy includes non-steroidal anti-inflammatory drugs and physical therapy. A soft lumbar corset is often prescribed in order to allow the back to have a chance to rest. If physical therapy, rest, and medications have failed to adequately relieve the symptoms of pain, over a significant period of time, surgical techniques such as spinal fusion or disc arthroplasty may be employed.

Fusion is currently the primary surgical intervention and consists in removing the degenerated disc (discectomy) and fusing (joining) the two adjacent vertebrae together to stop them from moving against each other (Figure 6 left). This is done by placing bone grafts or bone graft substitutes between the affected vertebral bone. However, a shortcoming of this invasive technique is that it reduces mobility and transfers stresses to the adjacent discs, which may potentially cause accelerated failure of the adjacent discs in turn [4].

Disc arthroplasty involves inserting an artificial disc into the intervertebral space after the natural defective disc has been removed (Figure 6 right). An artificial disc is a prosthetic device designed to maintain motion in the treated vertebral segment. It

acts like a joint, allowing for flexion, extension, side bending and rotation. However, disc arthroplasty is also an invasive procedure and issues related to device wear and compatibility with the surrounding tissue present other shortcomings.

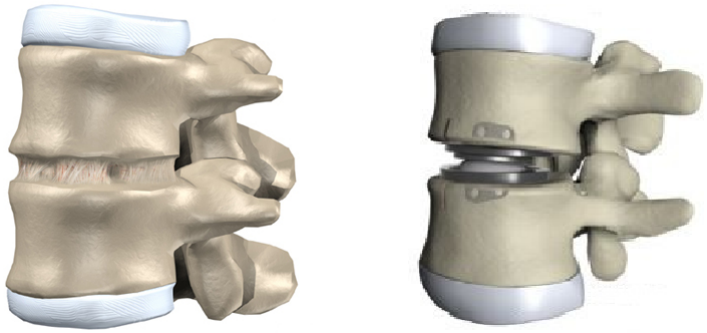

Figure 6: Surgical techniques to relieve pain due to disc degeneration: disc fusion (left) and disc arthroplasty (right)

2.2 Objective

The IVD has a very complex structure. This structure gives it a very complex mechanical behavior. Indeed, the IVD plays a significant role in the support, durability, and flexibility of the spine. It provides support and cushioning against mechanical loads. It is thus interesting to understand the mechanical properties of each component of the IVD, because each one contributes to the range of motion of the whole IVD. Otherwise, the IVD may undergo deep changes in structure and composition due to aging and/or pathological states. This phenomenon is known as disc degeneration. The reasons for disc degeneration are not well known, although external factors (such as mechanical overload on the spine) may be involved. But the underlying physical mechanism is not understood yet.

The long term objectives in the study of the IVD are:

1. being able to better understand the complex mechanical behavior of the IVD, the role and the properties of the different structure comprising the IVD and the relationship between them,

2. understanding the mechanism of disc degeneration.

In that purpose, it is interesting to use a finite element approach in order to create a model of the IVD. This model typically contains:

- multi-physics characteristics in order to accurately represent all the phenomena that occur in the IVD,

- a geometry of the IVD,
- material properties assigned to each component of the IVD,
- relevant boundary conditions and loading choices, so that the model would be able to reproduce macroscopic tests.

However, the time devoted to this master thesis is quite short (6 months) and the objectives mentioned above are ambitious. In order to fit the time allocated to this master thesis project, the objectives have to be reviewed. Consequently, the aim of this project will be the following:

- get used to a multi-physics modeling tool (COMSOL MULTIPHYSICS®[2]),
- make the first choices concerning the modeling of the intervertebral disc (physics, geometry, constitutive equations, boundary conditions and loading),
- run a few simulations of the model using COMSOL and derive a relevant analysis of the model according to the previous choices.

[2]For further reference, we will often use COMSOL instead of COMSOL MULTIPHYSICS® in order to simplify the writing.

3 State of the art

Several analytic and finite element models have been used to predict the behavior of the IVD, to investigate the process of disc degeneration, or to understand the complex exchange mechanisms in the IVD. The first chapter provides a description of some interesting models found in the literature as regards the physics, the geometry, the material properties, and the boundary conditions and loading. The second chapter is a brief summary of some important characteristics of the IVD that have to be taken into account for a modelisation of the disc. The third chapter deals with the modelisation of disc reconstruction.

3.1 Some models of the intervertebral disc

3.1.1 Physics

This chapter aims at describing the physical mechanisms occurring within the disc. Depending on the considered time-scale, the state of the IVD (healthy or degenerated) and the study which is carried out, some relevant physics characteristics have been emphasized.

In daily life, due to body weight, external loads, and forces exerted by the muscles, the intervertebral discs have to withstand high compressive loads, as well as bending and torsion.

Under short-term compression, the centered spherical NP, which has high water content, acts as a pillow and exerts a swelling pressure on the surrounding AF [14]. Pressure resulting from an applied load entails outwards bulging of the inner and outer margins of the AF [20, 21, 2]. Under compression, the AF withstands both compression and tension. The outward pressure applied to the AF predominantly causes hoop stresses along the circumference of the lamellae, placing the highly oriented fibers of the AF in tension. While the outer AF is in tension, axially as well as circumferentially, the inner AF bears some of the compressive loading axially [2]. The physics of the IVD under compression can be seen in Figure 7.

Whereas it has been shown that the short-term response was a fluid flow independent mechanism , long-term behavior (such as the study of diurnal cycles) exhibits the importance of fluid exudation and convective solutes transport for the adequate disc nutrition to be maintained [16]. Consequently, it has been shown that, after a recovery period, stiffness and disc height are fully restored [10, 23].

During aging and degeneration of the disc, the NP loses water. It can no longer perform its hydrostatic mechanical functions and becomes more solid-like. There-

fore, the stress distribution within the whole disc changes. The AF is no longer submitted to predominantly tensile stress but has to sustain compressive stresses directly. Several studies have been carried out to in order to understand the origin(s) of the phenomenon of disc degeneration. One interesting hypothesis [10] is that a deficiency in the nutrient supply (chemical origin) to the disc may be a contributing factor in disc degeneration. This deficiency may be caused by a decrease in the volume of fluid exchanged and the changes of pressure within the NP resulting from the diminution of its proteoglycans content, the decreased permeability of the endplates, and/or the possible presence of micro-cracks in the IVD structure. This puts in evidence the strong coupling between mechanical and chemical phenomena.

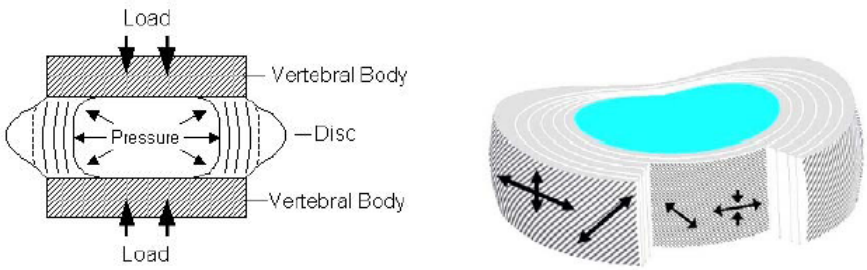

Figure 7: Behavior of a healthy IVD under compressive loading (arrows indicate approximate direction and magnitude)

3.1.2 Geometry

In general, the geometry of the disc has been simplified, and most of the studies have considered a generic geometry representing an average disc. A number of authors have assumed the structure to be axisymmetric [20, 21, 19] or to exhibit symmetry in either the sagittal or sagittal and transverse planes [23]. In many cases, the cranial and caudal surfaces of the disc have also been assumed to be flat.

The geometric dimensions have been taken from either in vitro measurements or medical image data such as magnetic resonance imaging (MRI) or computed tomography (CT). In the latter case, some dimensions have to be assumed or interpolated because of the lack of clear differentiation between the disc tissues under X-ray imaging [17].

The generation of the finite element mesh of the disc morphology is relatively straight-forward: in most cases, the disc can be meshed using automated methods so that the element size is approximately uniformly distributed.

3.1.3 Material properties

The intervertebral disc is a complex structure, and its behavior is governed by its biochemical as well as mechanical composition. Simulation of the disc function is therefore challenging and has led to the development of a number of different approaches to represent its behavior.

For relatively simple purposes, the NP has often been modeled as a non-linear incompressible solid governed by a Mooney-Rivlin law [4] or a fluid [20, 21, 22], while the AF was modeled as a homogeneous, isotropic, linear-elastic solid [4, 21, 20].

However, the highly layered and oriented structure of the AF suggests that its material behavior may be significantly anisotropic. The anisotropic behavior of the AF can be taken into account through discrete representation of the collagen fibers embedded within a homogeneous [18] or hyperelastic [22] matrix (the ground substance).

In recent years, increasing complexity has been incorporated into the material models used to represent the IVD tissue including (besides the anisotropy of the AF due to collagen fiber orientation) the fluid content and fluid flow, the osmotic forces and the regional variations in tissue composition. It must be known that, in simulating the AF behavior, anisotropic models alone may be sufficient to represent the instantaneous response of the IVD. However, simulation of the time-dependent response requires to consider the biphasic behavior of the tissue or the diffusion processes. For the first time in 1985, a poroelastic material behavior was introduced into a finite element model of the disc [25]. Both the AF and the NP were considered as biphasic, comprising an incompressible fluid phase that saturates and flows through an elastic isotropic solid phase. Transient and long-term creep finite element analysis included the study of deformation, pore fluid flow, stress, and pore fluid pressure, and it was shown that disc degeneration may be associated to an increase in discal permeability. Some authors [3] added material nonlinearities including stain-dependent permeability, and boundary pore pressure in order to analyze the poroelastic creep response under compression. Schroeder et al. [23] developed a fiber-reinforced poroviscoelastic swelling model (consisting in an elastic non-fibrillar solid matrix, a viscoelastic collagen fiber structure and an osmotically prestressed extrafibrillar fluid) to compute the interplay of osmotic, viscous and elastic forces under axial compressive load. They were able to show that loading of the disc tissue decreases the water content of the disc and that, following the load removal, the fluid content of the disc model reached the same condition as before loading.

3.1.4 Boundary conditions and loading

The global xyz coordinate system (which is shown in Figure 8) is set with the z-axis (axial direction) perpendicular to the mid-plane of the IVD, and the x- and y-axes being in the sagittal (positive toward posterior) and lateral (positive toward right) directions, respectively.

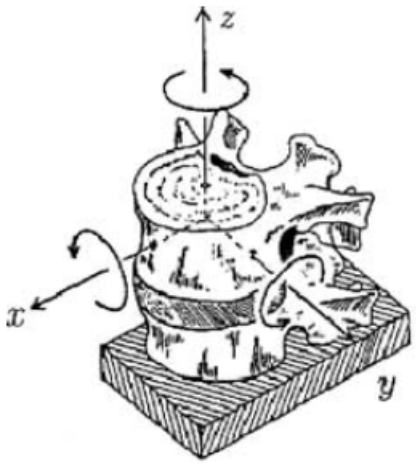

Figure 8: Global coordinate system usually associated to the IVD

Boundary conditions In general, the boundary conditions that are used are the following.

All the nodes along the top and bottom of the model are constrained in the x-direction to represent the attachment of the disk to the end-plates and vertebral bodies, and all the nodes along the bottom of the model are constrained in the y-direction (axial direction) to represent a rigid and fixed lower vertebral body [20, 21, 22, 8, 3].

When an axisymmetric model is considered, all the nodes along the central axis are constrained in the x-direction [20, 21].

Moreover, force exerted by the surrounding tissues is neglected on the outer boundary of the disc [23].

Loading Intervertebral discs have a primarily role in supporting body weight, transmitting loads through the spine, and allowing a great flexibility of the spinal column. During daily activities, IVDs are submitted to complex combination of static and cyclic loading, including large compressive loads or combined compression, flexion-extension, rotation. The majority of studies on spinal mechanics have focused

on the reproduction of relevant mechanical behavior of the spine.

Compression loading of the upper boundary of the IVD (or the upper vertebra when the study concerns a functional spinal unit) is the most spread study through literature. Baroud et al. [4] applied a displacement-controlled compression of 2.8 mm in a linear fashion so that the posterior endplate of L4 was displaced towards L5 in steps of approximately 0.2 mm. Meakin and Hukins [20] applied a pressure on the top of the model corresponding on a compressive load of 1.5 kN with compressive rate of 150 $N.s^{-1}$. Schroeder et al. [23] ran simulations under different loading steps: no axial loading, increasing axial load from 0 to 500 N over time, keeping a constant axial load of 500 N, increasing axial load from 500 to 1000 N over time, keeping a constant axial load of 1000 N, and decreasing axial load to 0.

Creep has also been studied by several authors in order to put in evidence the temporal response. In the study of Argoubi and Shirazi-Adl [3], the creep response is studied for a period of 2 h under a constant axial compression force of 400, 1200, or 2000 N. Ferguson et al. [10] simulated a diurnal loading cycle, consisting of an 8h resting period followed by 16h constant compressive load equivalent to 0.5 MPa average mechanical stress.

More complex loading have also been carried out. Rohlmann et al. [22] applied successively pure moments of 10Nm at the superior endplate simulating flexion, extension, lateral bending and axial rotation. Ehlers et al. [8] performed axial compression of 10% of the original height of the disc (0.144 mm) during 2.0 s followed by a rotation within 0.025 s.

3.2 Some results about the behavior of the intervertebral disc

The experimental results show some important characteristics of the IVD disc behavior.

Although it seems that the IVD may have an overall viscoelastic behavior, the NP and the AF show significant differences in their respective properties, and little is known about the individual contribution of each component to the overall mechanics of the IVD.

Regarding the type of loading which is applied on the IVD, the latter is able to exhibit different mechanical response. The strong anisotropy of the AF may have an important role in such a behavior.

In addition, since the mechanical response of the IVD time-dependent, a distinction must be made between an instantaneous response and long-term response according to the study which is carried out. While a “simple” model may be sufficient

to represent the instantaneous response of the IVD, some additional characteristics (diffusion, for example) have to be taken into account to represent the long-term response.

Eventually, while the mechanical role of the endplates is not well understood, they may have a significant contribution in the long-term response (nutriment supply).

3.3 How to model reconstruction ?

Interbody fusions and disc arthroplasty using intervertebral cages have become increasingly common in spinal surgery in order to alleviate the pain attributed to disc degeneration. Many studies report computational simulations of fusion and disc arthroplasty using the finite element method. Such simulations have been conducted in order to analyze how surgical technique may significantly affect the biomechanics of the spine: stress alteration of the disc adjacent to the anterior interbody fusion [7] or comparison of different cage designs in terms of their biomechanical interaction with the spinal structures [9] have been widely investigated.

Attempts to remove entirely the degenerated NP and to replace it have also been conducted and modeled using the finite element method, and reported through literature [20, 27]. The model of Meakin and Hukins [20] predicted that a full size implant would reverse the changes the behavior of the AF that are observed after denucleation whereas a smaller implant is not successful at returning the behavior of the AF to that of the intact disc. Also, by comparing the stress distribution in the AF, an ideal value of the Young's modulus was proposed. Yao et al. [27] also determined the optimal Young's modulus as well as the failure strength for the NP implant under different loading conditions, so that this implant is able to restore disc height and stress distribution under loading.

However, all those techniques are very invasive, and one of the challenges in designing a NP replacement component (in addition of being biocompatible and fatigue resistant) is that this component may be inserted using a minimally invasive or minimal access approach that limits destruction of surrounding tissue [11]. The NP replacement components currently under clinical investigation are three-dimensional, swellable polymers known as hydrogels. When placed in fluid, hydrogels can absorb water and also release water when loaded [6]. This ability may allow hydrogels to respond to compressive forces placed upon them, much like the native NP. Currently the nucleus replacement components are categorized as a preformed polymer (with a predetermined size and shape), an in situ curable polymer (the implant is injected

through a small annulotomy), or a combination (two examples of NP implants made of hydrogel can be seen in Figure 9). NP implants are still considered experimental, and many issues remain unanswered, such as whether these components will reliably recreate and maintain the viscoelastic properties of the native disc when subjected to multidirectional loads at differing rates.

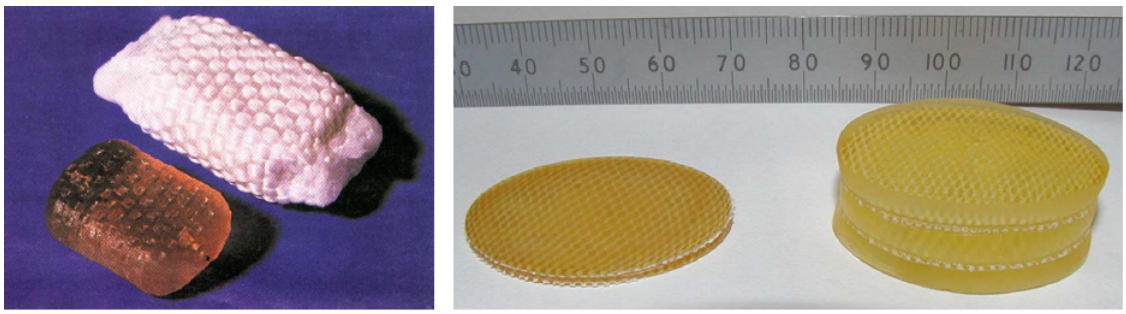

Prosthetic Disc Nucleus®

Neudisc® (pre- and post-hydration)

Figure 9: Examples of NP implants made of hydrogel

4 Basics of our intervertebral disc model

To determine stress and strain in biological soft tissues (such as the IVD), viscoelastic constitutive laws are often used in the context of finite element analysis. Moreover, it has been seen that the IVD is an incompressible structure which is subjected to high amplitude loads (Section 3.1.4). In the context of trying to understand the short-term response of the IVD, and the role the viscoelastic parameters of the NP and the AF, it is proposed, in the present work, to realize a finite element study together with a analytical study of *non-linear incompressible (large strain) viscoelasticity* while setting useful implementation tools for further studies. In that purpose, the constitutive framework of Huber and Tsakmakis [13] is used.

In the first section, a quick overview of the theory of viscoelasticity based on [13] is made. In the second section, the implementation of non-linear incompressible viscoelasticity at large strain in Matlab and COMSOL is described.

4.1 Non-linear incompressible viscoelasticity

4.1.1 General information about viscoelasticity

Viscoelasticity is the property of materials that exhibit both viscous and elastic characteristics when undergoing deformation. Viscous materials resist shear flow and strain linearly with time when a stress is applied. Elastic materials strain instantaneously when stretched and just as quickly return to their original state once the stress is removed. Viscoelastic materials have elements of both of these properties and, as such, exhibit time dependent strain.

A viscoelastic material has the following properties:

- hysteresis: the amount of dissipated energy is the area of hysteresis loops (Figure 10); it reflects the damping properties of the material,
- stress relaxation occurs: step constant strain causes decreasing stress (Figure 11),
- creep occurs: step constant stress causes increasing strain up to a given limit, if the material behaves like a solid (Figure 11).

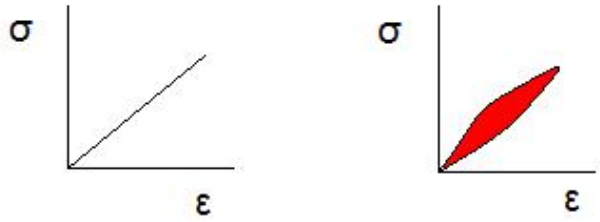

Figure 10: Stress-strain response of an elastic material (left) and a viscoelastic material showing hysteresis (right)

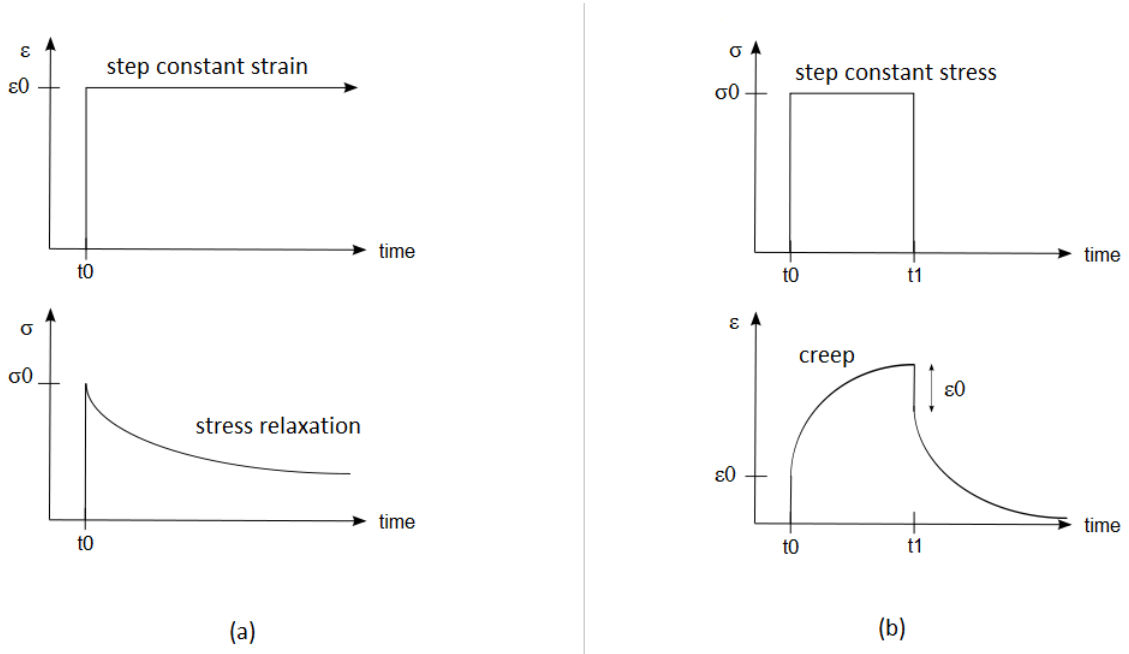

Figure 11: Viscoelastic stress relaxation in response to a step constant strain ε_0 (a) and creep in response to a step constant stress σ_0 (b)

Viscoelastic materials can be modeled in order to determine their stress or strain interactions as well as their temporal dependencies using a linear combination of springs and dashpots to represent elastic and viscous components, respectively. These models, which include the Maxwell model (a spring and a dashpot in series), the Voigt model (a spring in parallele with a dashpot), and the so-called Zener model (Figures 12 and 13), are used to predict a material's response under different loading conditions. Maxwell model and Voigt model are commonly used. However, these models are often proved to be insufficient: the Maxwell model describes linear creep and stress relaxation, and the Voigt model does not describe creep, neither stress relaxation (under constant strain). The Zener model is the simplest model that predicts both phenomena. It is composed of a spring in series with a Maxwell

element (Figure 13).

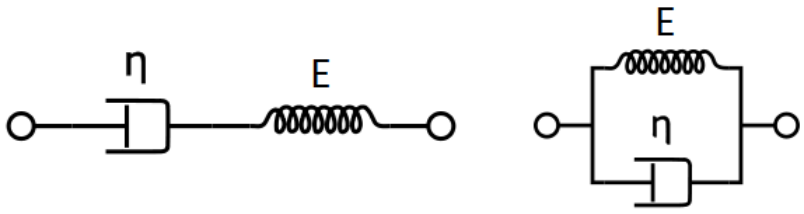

Figure 12: Maxwell model - spring and dashpot in series (left); Voigt model - spring and dashpot in parallel (right)

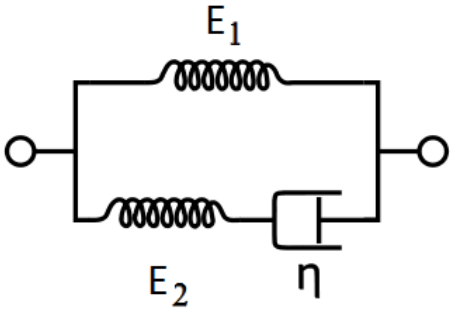

Figure 13: Zener model - spring in series with a Maxwell element

4.1.2 Linear viscoelasticity

Linear viscoelasticity is when the response function (strain or stress) is separable in both creep response and load. It is usually applicable only for small deformations.

The elastic components, as previously mentioned, can be modeled as springs of elastic constant E, given the formula:

$\sigma = E\varepsilon$, where σ is the stress, E is the elastic modulus of the material, and ε is the strain that occurs under the given stress, similar to Hooke's Law.

The viscous components can be modeled as dashpots such that the stress-strain rate relationship can be given as:

$\sigma = \eta\dot{\varepsilon}$, where σ is the stress, η is the viscosity of the material, and $\dot{\varepsilon}$ is the time derivative of strain.

For the Zener model, the governing constitutive relation is:

$$\dot{\sigma} + \frac{E_2}{\eta}\sigma = (E_1 + E_2)\,\dot{\varepsilon} + \frac{E_1 E_2}{\eta}\varepsilon \tag{1}$$

4.1.3 Non-linear viscoelasticity

Non-linear viscoelasticity is when the response function (strain or stress) is not separable in both creep response and load. It usually happens when the deformations are large or if the material changes its properties under deformations.

To derive the mechanical response of the large strain viscoelastic model, according to Huber and Tsakmakis [13], a multiplicative decomposition of the deformation gradient tensor

$$\mathbf{F} = \mathbf{F}_e \mathbf{F}_i \tag{2}$$

can be used (Figure 14). The part $\mathbf{F}_i$ is the inelastic part of the deformation gradient which transforms the body from the reference configuration (C_0) to an intermediate equilibrium configuration (C_i). It is important to note that this decomposition is not unique. It is a conceptual one, and can generally not be determined experimentally. Here, intermediate equilibrium configuration (C_i) is chosen as a stress-free configuration which would be obtained by an infinitely fast unloading.

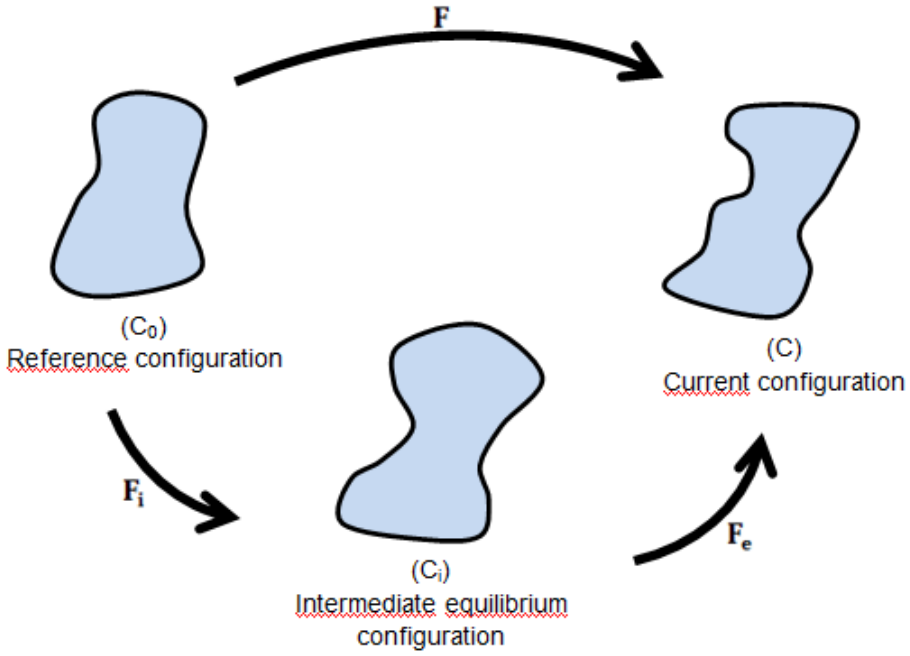

Figure 14: Multiplicative decomposition of the deformation gradient tensor

Within that multiplicative framework, it can be shown [13] that, under the assumption of incompressibility and using a neo-Hookean formulation for the non-linear springs, the constitutive equation governing the response of the model is

given by:

$$\sigma = -p\mathbf{I} + 2c_1\mathbf{b} + \mathbf{2}c_{1_e}\mathbf{b}_e \tag{3}$$

where

- σ is the Cauchy stress tensor of the deformation,
- p is the pressure,
- $\mathbf{I}$ is the identity tensor,
- c_1 and c_{1_e} are the neo-Hookean material constants of the "total" spring and the "elastic" spring respectively, supposing that the strain energy density of the model has the form $W = W_1(\mathbf{E}) + W_2(\mathbf{E}_e)$, with $W_1(\mathbf{E}) = c_1(I_1 - 3)$ for the "total" spring and $W_2(\mathbf{E}_e) = c_{1_e}(I_{1_e} - 3)$ for the "elastic" spring (I_1 and I_{1_e} being the first invariant of $\mathbf{F}$ and $\mathbf{F}_e$ respectively),
- $\mathbf{b} = \mathbf{F}\mathbf{F}^T$ is the left Cauchy-Green strain tensor associated to the total deformation,
- $\mathbf{b}_e = \mathbf{F}_e\mathbf{F}_e^T$ is the left Cauchy-Green strain tensor of the elastic part and is governed by the following evolution equation:

$$\dot{\mathbf{b}}_e = \mathbf{b}_e\mathbf{l}^T + \mathbf{l}\mathbf{b}_e - \frac{4c_{1_e}}{\eta}\mathbf{b}_e\mathbf{dev}(\mathbf{b}_e) \tag{4}$$

with $\mathbf{l} = \dot{\mathbf{F}}\mathbf{F}^{-1}$ the spatial velocity gradient tensor, $\mathbf{dev}(\mathbf{b}_e) = \mathbf{b}_e - \frac{1}{3}tr(\mathbf{b}_e)\mathbf{I}$ the deviatoric part of tensor $\mathbf{b}_e$, and η the material viscosity.

Finally, the mechanical problem that we want to solve is given by:

- the equilibrium equations: $\overrightarrow{\mathbf{div}}(\sigma) = \overrightarrow{\mathbf{0}}$ on Ω (in the absence of external applied forces),
- the boundary conditions: $\sigma.\vec{\mathbf{n}} = \overrightarrow{0}$ on $\partial_\sigma\Omega$ and $\overrightarrow{\mathbf{u}} = \overrightarrow{\mathbf{u}_{imp}}$ on $\partial_u\Omega$.

However, the local form of the governing equations of a continuum mechanics problem it is not appropriate from a computational point of view. The variational principle allows us to obtain an integral form or weak form of the local form of the governing equations of a continuum mechanics problem. A variational (weak) form for any set of equations is a scalar relation and may be constructed by multiplying the equation set by an appropriate arbitrary function, integrating over the domain of the problem and setting the result to zero. Here, the arbitrary function is a virtual

displacement $\delta\vec{\mathbf{u}}$. Thus, the weak form associated to the present problem (in the absence of external applied forces) is:

$$\int_{\Omega} \sigma : \mathbf{grad}\,(\delta\vec{\mathbf{u}})\, d\Omega = 0 \tag{5}$$

or equivalently:

$$\int_{\Omega_0} \mathbf{P} : \mathbf{grad}\,(\delta\vec{\mathbf{u}})\, d\Omega = 0 \tag{6}$$

where Ω is the deformed domain of the problem (in the current configuration), Ω_0 is the reference (undeformed) domain, and $\mathbf{P} = J\sigma\mathbf{F}^{-T}$ is the first Piola-Kirchhoff stress tensor.

4.2 Numerical procedure

Non-linear incompressible viscoelasticity at large strain was implemented in two ways. First, an analytical model was created in Matlab in order to understand the behavior of those equations on a homogeneous uniaxial traction test. This model is intended to serve as a reference to check and validate the implementation of the same law in COMSOL. Then, viscoelasticity at large strain was implemented in COMSOL in three dimensions and in an axisymmetic frame.

4.2.1 1D analytical model using Matlab

This chapter describes how non-linear incompressible viscoelasticity at large strain was implemented in Matlab. The goal is to compute the theoretical stress response of the non-linear incompressible viscoelastic rheological model submitted to an uniaxial traction test.

Assuming that simple tension is applied along $\overrightarrow{\mathbf{e}_1}$ direction and assuming incompressibility of the material, the deformation gradient tensor can be written as:

$$\mathbf{F} = \begin{bmatrix} \lambda & 0 & 0 \\ 0 & \frac{1}{\sqrt{\lambda}} & 0 \\ 0 & 0 & \frac{1}{\sqrt{\lambda}} \end{bmatrix}$$

where λ (ratio between deformed and undeformed length of the specimen) is the imposed time-dependent loading.

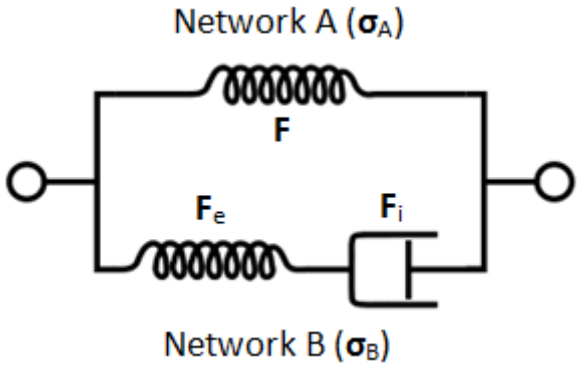

Figure 15: Illustration of the multiplicative deformation gradient decomposition on the viscoelastic model

At instant $t = 0$, the inelastic part of the deformation gradient is initiated to identity.

At each time step, λ is computed; then the deformation tensor,$\mathbf{F}$, and the stress in network A (Figure 15) comprised of the spring alone, σ_A, are calculated. The inelastic part of network B (comprised of the spring and dashpot in series as depicted in Figure 15), λ_i, is set to its previous value, and the elastic part is computed using $\lambda_e = \frac{\lambda}{\lambda_i}$. The elastic deformation tensor,$\mathbf{F}_e$, and the stress in network B, σ_B, are estimated. Finally, a new value of λ_i is computed using Euler method to express $\mathbf{F}_i$ in terms of its previous value and the expression of the strain rate tensor $\mathbf{d}_i$ (A). The new value of λ_i is compared to the previous one. If the error is negligible, then the new value of λ_i is accepted. If the error is greater than the error limit, then the value of λ_i is stored and a loop is made. Refer to Appendix B to see the entire Matlab program.

4.2.2 3D and axisymmetric (2D) models using COMSOL

General information about COMSOL Multiphysics COMSOL Multiphysics is a finite element software based on the solving of any PDE problems and aimed to be as general as possible in this domain. Its strength is to enable the implementation and solving for any set of coupled PDE problems, for any user-chosen interpolation. It also offers some already implemented classical physics such as non-linear mechanics for large strain problems that will be used in this work. This last module provides several hyperelastic models such as the neo-Hookean and Mooney-Rivlin ones, and new models can be quite easily implemented by simply giving user-defined strain energy functions (see for example [5]). For a better understanding of what follows, the reader should be familiar with the concepts and elementary vocabulary

of COMSOL Multiphysics which can be accessed at http://www.comsol.com/.

3D model using COMSOL This chapter describes step by step how non-linear incompressible viscoelasticity at large strain is implemented in COMSOL. For simplicity, the geometrical description will focus on the homogeneous 3D tension test depicted above, but could be applied to any other geometry.

The space variables are 'x', 'y' and 'z'.

Multiphysics In order to describe the problem defined in Section 4.1.3, two application modes and modules are required for the model:

- Solid, Stress-Strain (Structural Mechanics module), with the three displacement variables 'u', 'v', 'w' as independent variables;
- PDE, General Form, where nine independent variables are needed ('Bexx_1', 'Bexy_1', 'Bexz_1', 'Beyx_1', 'Beyy_1', 'Beyz_1', 'Bezx_1', 'Bezy_1', 'Bezz_1') representing the nine components of $\mathbf{b}_e$.

Geometry modeling For the further validation of the model, the geometry which is used here is a $1 * 1 * 20$ mm^3 box.

Constants and expressions settings In the constants settings, all the constants of the problem, such as the material constants (c_1, c_{1_e} and η) and other input data for the model, are defined. In the expression settings, mathematical expressions that are involved in the evolution equation (8) and other useful expression are defined.

Typically, the time derivative of deformation gradient $\dot{\mathbf{F}}$, the spatial velocity gradient tensor $\mathbf{l}$, and the deviatoric part of the left Cauchy-Green elastic strain tensor $\mathbf{dev}\,(\mathbf{b}_e)$ are defined as functions of the displacement and pressure (which is introduced hereafter in the Structural mechanics subdomain settings) variables in order to define the right-hand side of equation (8) as a "source term". Eventually, the first Piola-Kirchhoff stress tensor which is useful for the definition of the weak problem is expressed. The table of expressions settings can be seen in Appendix C.

Physics modeling In this step, all the descriptions and settings for the physics and equations of the model are entered. For each application mode (Structural mechanics mode and PDE mode), the subdomain settings (material properties, sources,

PDE coefficients, initial condition and element types on the subdomains) and the boundary settings (boundary and interface conditions) are specified.

Structural mechanics settings

Subdomain settings At first, a hyperelastic material is chosen for the box subdomain. This enables us to define a comprehensive framework that is fairly close to what we want to work with, and for which only a few details will be performed in order to achieved the accurate formulation of the non-linear viscoelastic law.

Moreover, a so-called mixed formulation has to be used. Indeed, when the viscous strains grow large, the near incompressibility can cause numerical problems if only displacements are used in the interpolating functions. In a mixed formulation, the pressure 'p' is introduced as a new independent variable within the Structural Mechanics mode.

The mechanical problem is defined using the weak form (6), which may be written in 3D as:

$$\iiint_{\Omega_0} (P_{xx}\delta u_{,x} + P_{xy}\delta u_{,y} + P_{xz}\delta u_{,z} + P_{yx}\delta v_{,x} + P_{yy}\delta v_{,y} + P_{yz}\delta v_{,z} +$$

$$P_{zx}\delta w_{,x} + P_{zy}\delta w_{,y} + P_{zz}\delta w_{,z} + \delta p\,(J-1))\,dxdydz = 0 \tag{7}$$

In COMSOL, the quantity under the integral sign is written:

```
ux_test*Px_smsld+uy_test*Pxy_smsld+uz_test*Pxz_smsld
+vx_test*Pyx_smsld+vy_test*Py_smsld+vz_test*Pyz_smsld
+wx_test*Pzx_smsld+wy_test*Pzy_smsld+wz_test*Pz_smsld
+p_test*(J_smsld-1)
=0
```

In the expression above, the particle '_test' refers to the virtual function of the weak form, J is the determinant of the deformation gradient tensor. 'Px_smsld', 'Pxy_smsld', ..., 'Pz_smsld' refer to the nine components of the first Piola-Kirchhoff stress tensor which values have to be modified in order to respect the formulation of non-linear viscoelasticity at large strain through the expressions that have been properly defined in the scalar expressions settings section (Table 1).

Name	Expression	Description
Px_smsld	PK1xx_1	First Piola-Kirchhoff stress tensor xx component
Pxy_smsld	PK1xy_1	First Piola-Kirchhoff stress tensor xy component
Pxz_smsld	PK1xz_1	First Piola-Kirchhoff stress tensor xz component
Pyx_smsld	PK1yx_1	First Piola-Kirchhoff stress tensor yx component
Py_smsld	PK1yy_1	First Piola-Kirchhoff stress tensor yy component
Pyz_smsld	PK1yz_1	First Piola-Kirchhoff stress tensor yz component
Pzx_smsld	PK1zx_1	First Piola-Kirchhoff stress tensor zx component
Pzy_smsld	PK1zy_1	First Piola-Kirchhoff stress tensor zy component
Pz_smsld	PK1zz_1	First Piola-Kirchhoff stress tensor zz component

Table 1: Changes needed in the subdomain settings in order to take into account the right expression of the first Piola-Kirchhoff stress tensor (3D case)

Boundary settings The bottom and left boundaries are constrained to be symmetric in order to have a homogeneous test case. On the top boundary, a displacement is imposed. All the other boundaries are left free. The mechanical boundary conditions are illustrated in Figure 16.

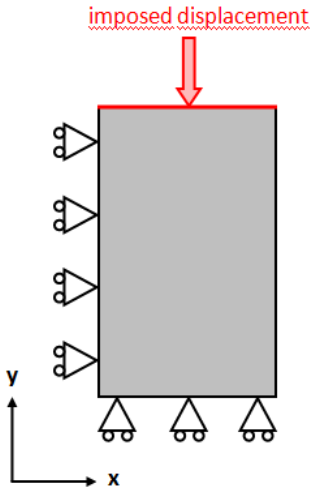

Figure 16: Mechanical boundary conditions of the homogeneous test case

PDE, settings

Subdomain settings The equation that is to solve is the following evolution equation (8):

$$\dot{\mathbf{b}}_e = \mathbf{f}(\mathbf{b}_e, \mathbf{l}) \tag{8}$$

where $\mathbf{f}(\mathbf{b}_e, \mathbf{l}) = \mathbf{b}_e\mathbf{l}^T + \mathbf{l}\mathbf{b}_e - \frac{4c_{1_e}}{\eta}\mathbf{b}_e\mathbf{dev}\left(\mathbf{b_e}\right)$ is the "source term" which has been properly defined in the scalar expressions settings (Appendix C).

Boundary settings Neumann boundary conditions with a zero flux are imposed on all the boundaries, so that Equation 8 is equivalent to a local equation which would be solved at integration points in a standard FEM code. The structure of COMSOL imposes this type of ODE to be treated as a field equation (like any PDE). This, of course, plants a problem regarding the compatibility of interpolations of both coupled problems as $\mathbf{b}_e$ should be interpolated as the gradient of the displacement field. As will show the results presented in chapter 5, the choice of an order 2 for displacements and order 1 for $\mathbf{b}_e$ seems to give good results.

Mesh generation The mesh is created using the free mesh parameters. It is automatically created so that the element size is approximately uniformly distributed.

Solver parameters Since the analysis is a transient-type analysis, a time-dependent solver has to be selected. A large number of possible solver are available in COMSOL Multiphysics [1]. The UMFPACK direct solver is the default linear system solver. It is the one which is selected here because it is known to be robust and it has proven to be quite fast for the present problem.

Axisymmetric (2D) model using COMSOL In this chapter, the COMSOL implementation of non-linear incompressible viscoelasticity at large strain is described in an axisymmetric (2D) framework. The procedure is very similar to the 3D case, but some particular attention has to be paid on a few details.

In the axisymmetric case, the analysis domain is a three-dimensional body of revolution defined in cylindrical coordinates 'r', 'phi' and 'z' in COMSOL, but deformations and stresses are two-dimensional functions of 'r' and 'z' only.

All relevant tensors are defined by only five components: the three diagonal components, rz component and zr component.

As previously, Solid, Stress-Strain (Structural Mechanics module) and PDE, General Form are chosen to describe the multiphysics problem. The independent variables are 'uaxi' (radial displacement), 'w' (axial displacement), and 'p' (pressure from mixed-formulation) for the Structural Mechanics module and 'Berr_1', 'Berz_1', 'Be22_1', 'Bezr_1', 'Bezz_1' (representing $\mathbf{b}_{e_{rr}}$, $\mathbf{b}_{e_{rz}}$, $\mathbf{b}_{e_{\varphi\varphi}}$, $\mathbf{b}_{e_{zr}}$, $\mathbf{b}_{e_{zz}}$ respectively) for the PDE, General Form mode.

While the constant settings remain the same as in 3D, the expression settings change due to the axisymmetric formulation (Appendix C).

The mechanical problem is defined using the weak form (6), which may be written in the axisymmetric case as:

$$\iint_{\Omega_0} 2\pi \left(P_{rr}\delta u_{,r} + P_{rz}\delta u_{,z} + P_{\varphi\varphi}\frac{\delta u}{r} + P_{yx}\delta v_x + \right.$$

$$\left. P_{zr}\delta w_{,r} + P_{zz}\delta w_{,z} + \delta p\,(J-1) \right) r dr d\varphi = 0 \tag{9}$$

In COMSOL, the quantity under the integral sign is written:

```
2*pi*r*(uaxir_smaxi_test*Pr_smaxi+uaxiz_smaxi_test*Prz_smaxi
+uor_test*Pphi_smaxi+wr_test*Pzr_smaxi+wz_test*Pz_smaxi
+p_test*(J_smaxi-1))=0
```

In the expression above, the particle '_test' still refers to the virtual function of the weak form. 'uor' is defined as the radial displacement 'uaxi' divided by 'r', and J is the determinant of the deformation gradient tensor. As for the 3D case, the five components of the first Piola-Kirchhoff stress tensor ('Pr_smaxi', ..., 'Pz_smaxi') have to be modified in order to respect the formulation of non-linear viscoelasticity at large strain through the expressions that have been properly defined in the scalar expressions settings section (Table 2).

Name	Expression	Description
Pr_smaxi	PK1rr_1	First Piola-Kirchhoff stress tensor rr component
Prz_smaxi	PK1rz_1	First Piola-Kirchhoff stress tensor rz component
Pphi_smaxi	PK122_1	First Piola-Kirchhoff stress tensor $\varphi\varphi$ component
Pzr_smaxi	PK1zr_1	First Piola-Kirchhoff stress tensor zr component
Pz_smaxi	PK1zz_1	First Piola-Kirchhoff stress tensor zz component

Table 2: Changes needed in the subdomain settings in order to take into account the right expression of the first Piola-Kirchhoff stress tensor (axisymmetric case)

Finally, the evolution equation equation $\dot{\mathbf{b}}_e = \mathbf{f}(\mathbf{b}_e, \mathbf{l})$ has to be solved paying attention to the axisymmetric formulation of the source term $\mathbf{f}(\mathbf{b}_e, \mathbf{l}) = \mathbf{b}_e\mathbf{l}^T + \mathbf{l}\mathbf{b}_e - \frac{4c_{1_e}}{\eta}\mathbf{b}_e\mathbf{dev}\,(\mathbf{b_e})$ (defined in the scalar expressions settings as can be seen in Appendix C).

5 Results

This section aims at analyzing the meaning of the non-linear large strain viscoelastic law in terms of its parameters.

In the first section, the influence of each parameter is investigated using the 1D analytical Matlab model. Then, in the second section, the implementation in COMSOL is validated using the comparison with the 1D analytical Matlab model. In the last section, some simulations of the IVD behavior using non-linear incompressible viscoelasticity are run.

5.1 Analysis of the model

As seen in Section 4.1.3, non-linear incompressible viscoelasticity involves three material parameters: c_1, c_{1_e} (the neo-Hookean material constants associated to the "total" spring and the "elastic" spring respectively), and η representing the viscosity of the material. Thus, two characteristic times can be defined:

- $\tau_e = \frac{\eta}{c_{1_e}}$ which would be the time required to get a purely viscous response in the viscoelastic branch (it would control the "local" viscoelastic effects),

- $\tau = \frac{\eta}{c_1}$ which would be the characteristic time to get the elastic response given by c_1.

In order to investigate the role of each parameter, the 1D theoretical Matlab model is used (refer to Section 4.2.1 and Appendix B): several cases are run, keeping fixed two parameters while the third one varies. The loading history $\lambda(t)$ is chosen to be triangular (Figure 17) to represent a loading-unloading cycle with a stretch amplitude of 0.5 and a strain rate of 0.05 s^{-1}, that means a loading characteristic time $\tau_{load} = 20$ s.

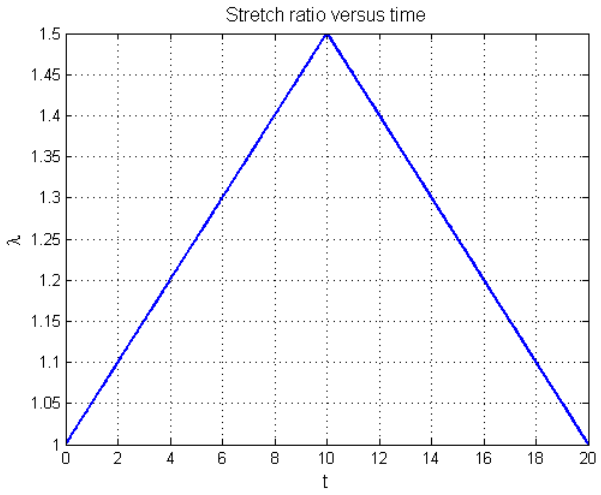

Figure 17: Strain history $\lambda(t)$: triangular input loading

Figures 18, 19, and 20 show the influence of τ, τ_e, and η respectively on the stress response. According to Figure 18, we can see that for any value of τ, the stress response reflects a purely elastic test: non-linear effects are not visible, but this is due to the fact that λ is rather small. Moreover, there is a great axial stress increase while τ decreases (or while c_1 increases), and no hysteresis effect is observed. Thus, we can deduce that parameter c_1 acts directly on the stiffness of the model. Figure 19 shows that hysteresis increases as τ_e decreases (or, equivalently, when c_{1_e}increases). The calculation is made setting c_1 to zero, which results in a viscoelastic Maxwell (fluid type) behavior of the material. For the case where $\tau_e = 0.1 \ll \tau_{load}$, the obtained response is an almost viscous response and the stress is directly linked to the loading velocity (that is why the curve reaches a maximum value and then decreases). For the case where the characteristic time are of the same order of magnitude ($\tau_e = 10 \approx \tau_{load}$), the obtained response is that of a typical viscoelastic fluid response. Eventually, for the case where $\tau_e = 1000 \gg \tau_{load}$, the obtained response is an almost elastic response.

Figure 20 shows that the axial stress and the hysteris effect increase while η increases. Thus, parameter η acts both on the stiffness response of the model and on the energy dissipation properties of the material.

To conclude on the meaning of each parameter, one could say that c_1 gives the global stiffness (and the long time instantaneous response), c_{1_e} and η control the viscoelastic behavior. Two characteristic times can be defined for this model: τ_e controls the "local" viscoelastic effects, i.e. the time necessary to get a purely viscous response in the viscoelastic branch, and τ represents the characteristic time to get the elastic response given by c_1.

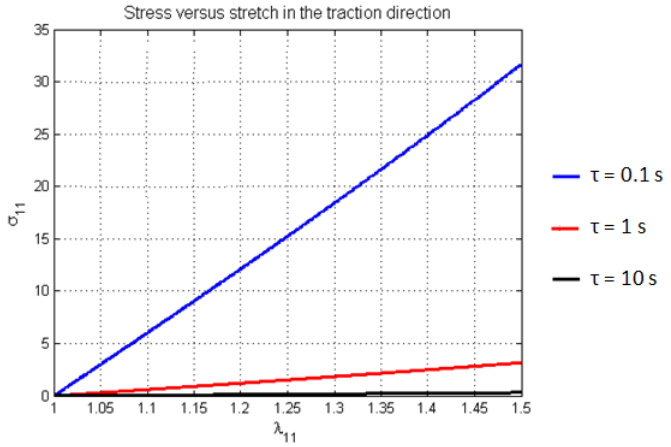

Figure 18: Influence of parameter τ ($c_{1_e} = 0$ and $\eta = 1$ fixed)

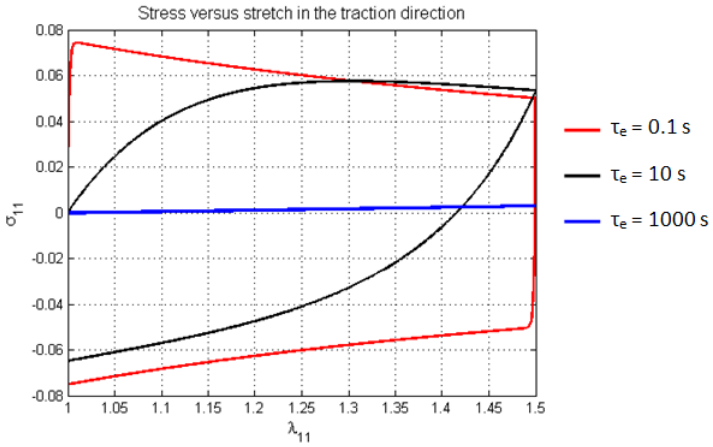

Figure 19: Influence of parameter τ_e ($c_1 = 0$ and $\eta = 1$ fixed)

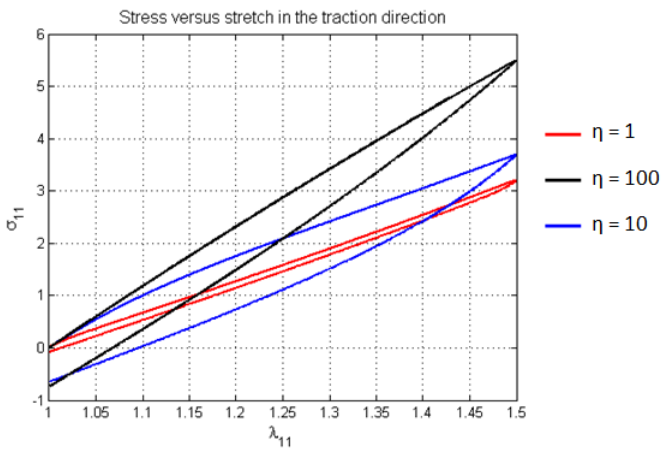

Figure 20: Influence of parameter η ($c_1 = 1$ and $c_{1_e} = 1$ fixed)

Keeping in mind the context of the IVD modelisation, one could imagine that such a model describes the macroscopic behavior of and elastic material (network of elastic collagen fibers) surrounded by a viscoelastic fluid (groundsubstance). The fluid may be responsible for stress overshoots in case of very fast loading but, contrary to a simple Voigt model, will always lead to a finite value thanks to the elastic part c_{1_e}. In case of very slow loading, only the "macroscopic" elasticity will play a role.

5.2 Validation

Based on the theory of Huber and Tsakmakis [13], non-linear incompressible viscoelasticity at large strain was implemented in two ways: an analytical model was created in Matlab (refer to Section 4.2.1 and Appendix B) and a finite element model was implemented in COMSOL. However, the implementation using COMSOL may be quite tricky (as it was shown in Sections 4.2.2 and 4.2.2). In order to be sure that the law has been correctly implemented, a comparison with the 1D analytical model (whose results are much more reliable) is needed. In that purpose, a simple homogeneous case was designed and a traction-compression test has been performed both in Matlab and COMSOL.

Different loading cases were investigated, simulating a loading-unloading cycle: a triangular input loading and a sinusoidal input loading were tested (for the stretch ratio λ versus time), making the amplitude of the signal and the stretch rate vary. In addition, several sets of parameters (c_1, c_{1_e} and η) were investigated in both codes. The comparisons were performed on the axial stress response versus time and on the axial stress versus axial stretch.

For instance, the theoretical (Matlab) model response to the strain history defined in Figure 17 is presented in Figure 21; the COMSOL model response to the same input loading is presented in Figure 22. For this calculation, the stretch amplitude is fixed to 0.5 while the strain rate is fixed to 0.05 s^{-1}, as can be seen on Figure 17. That means that the size of the specimen in the traction direction is increased by half when the stretch is at its maximum value. In the COMSOL model, the specimen is 20 mm long initially and reaches 30 mm when the stretch is at its maximum value. The results obtained here correspond to the following set of parameters: $c_1 = 0.1$, $c_{1_e} = 0.1$ and $\eta = 10$.

A very good match can be observed between the theoretical results obtained with Matlab and the results obtained with COMSOL. The same trend is observed for any set of parameter and any loading case. Thus, it can be concluded that the

implementation of non-linear incompressible viscoelasticity at large strain has been correctly performed in COMSOL.

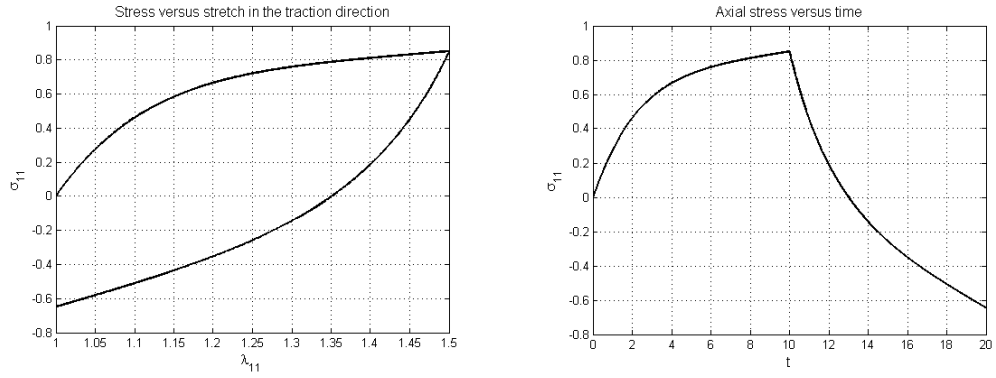

Figure 21: Theoretical (Matlab) model response: axial stress versus axial stretch (left) and axial stress response versus time (right)

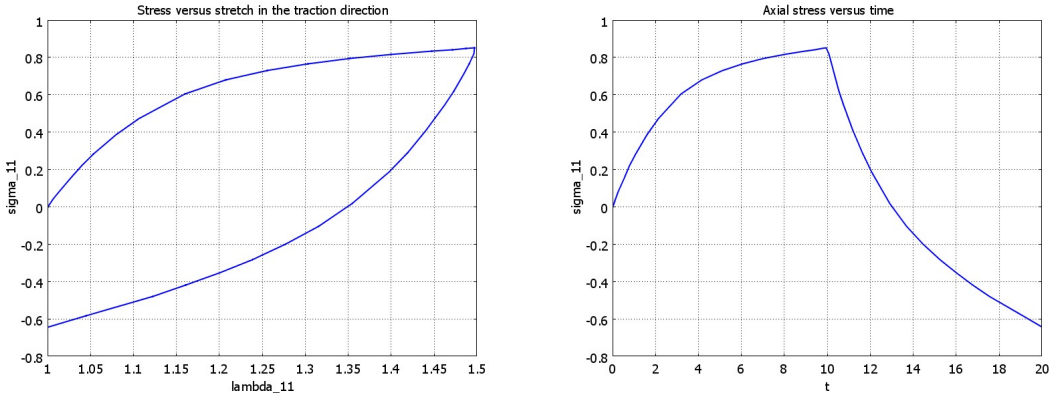

Figure 22: COMSOL model response: axial stress versus axial stretch (left) and axial stress response versus time (right)

5.3 First simulations

In this section, a few simulations of the IVD behavior using non-linear incompressible viscoelasticity for both the AF and the NP are run. The model is assumed to have an axisymmetric geometry.

5.3.1 Axisymmetric model

Geometry description The geometry of the intervertebral disc (both AF and NP) was approximated to be cylindrical. This approximation meant that the geometry could be described in terms of just three parameters: height, disc radius, and

nucleus radius. The dimensions of the model were those used by Meakin [20, 21]: 12 mm for the NP radius, 23 mm for the disc radius and 12 mm for the height of the disc (Figure 23). Those values were shown to be reasonable for a typical human lumbar disc [20].

Boundary conditions and loading The nodes along the central axis were constrained in r-direction (radial direction) for axisymmetry to be maintained. The nodes along the top and bottom of the model were constrained in r-direction to represent the attachment of the disc to the endplates and vertebral bodies, thus assumed infinitely rigid with respect to the IVD. The nodes along the bottom of the model were constrained in z-direction (axial direction) to represent a rigid and fixed lower vertebral body. The boundary conditions are depicted in Figure 23. A imposed displacement was prescribed on the upper boundary of the model.

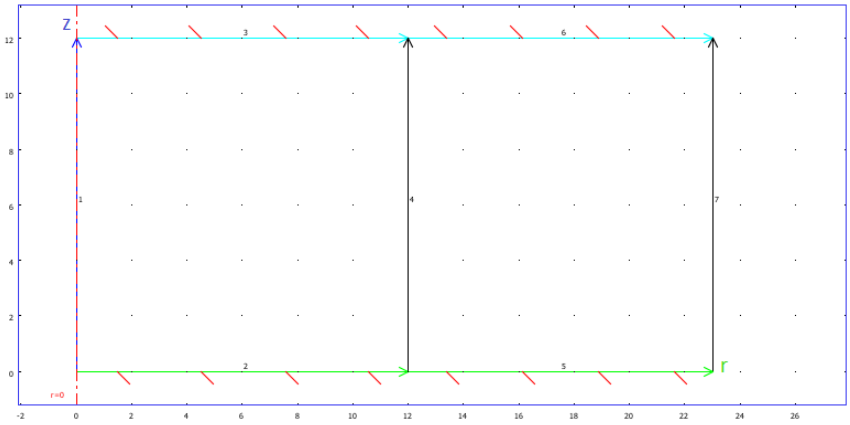

Figure 23: Geometry and boundary conditions (axisymmetric, cylindrical model)

5.3.2 Simulations

Non-linear incompressible viscoelasticity, which is characterized by three material parameters, was used for the AF and the NP, which results in a set of 6 material parameters for the whole model of the IVD. However, due to a lack of time, full sensitivity analysis (varying the value of each input parameter individually and observing the output) could not be performed. Only a few tests were carried out with different sets of parameters, which were supposed to be relevant, according to the analysis of the model performed on the 1D analytical case in Section 5.1.

Influence of the loading characteristic time First, the influence of the loading characteristic time τ_{load} was investigated. Figure 25 presents the force along z-

direction versus time response of the model to the two different loading times defined in Figure 24. The component of the force along r-direction is negligible.

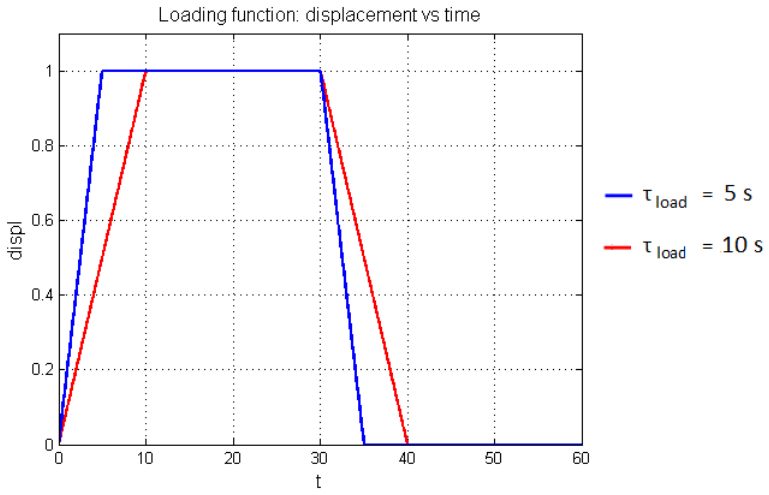

Figure 24: Imposed displacement applied on the top boundary of the IVD for different loading characteristic time τ_{load}

It can be seen that the force response gets faster when the loading characteristic time is smaller. Anyway, for both cases, the force response curve presents the same trend: a constant value of about -14 kN is reached for the stress when the imposed displacement is constant with a small time delay (peak) compared to the displacement versus time curve, then the state of 0 force is recovered when the displacement returns to 0, again with a small time delay. The viscoelastic behavior of the model is thus put in evidence.

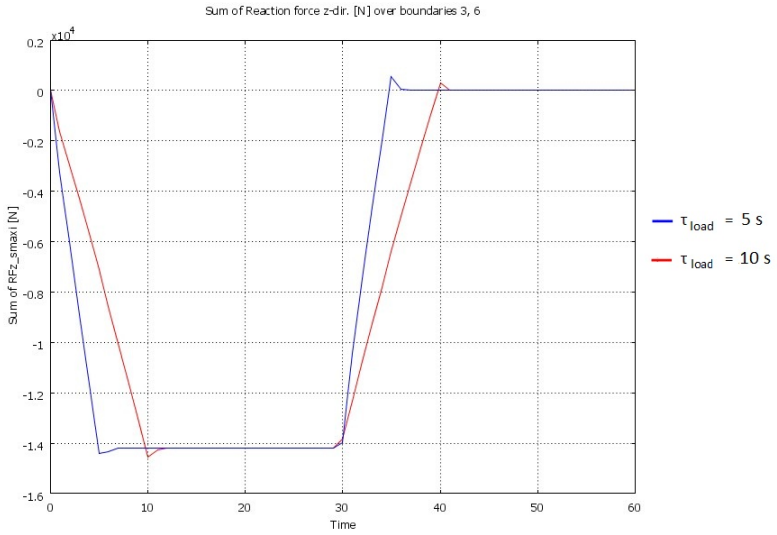

Figure 25: Influence of the loading characteristic time τ_{load} on the force (along z-direction) versus time response of the model (all the material parameters being fixed to the value of 1)

For a loading characteristic time $\tau_{load} = 10$ s, and for all the material parameters fixed to the value of 1, the map of the total displacement is displayed in Figure 26 and the pressure distribution within the disc is presented in Figure 27. From those figures, we can see that the NP pushes the AF outwards under load (1.5 mm in the radial direction) because the pressure within the NP is greater than the pressure within the AF. This reflects the typical behavior of a healthy IVD.

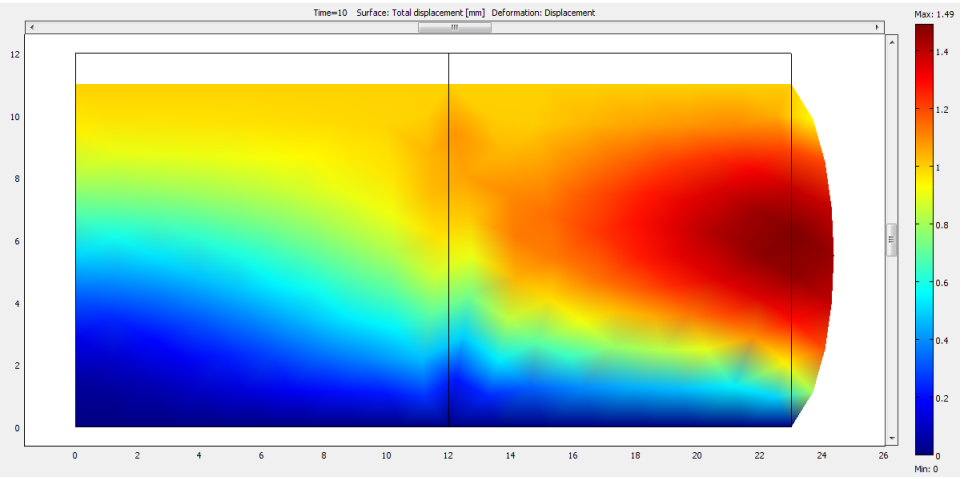

Figure 26: Total displacement within the IVD ($c_1^{NP} = 1$, $c_{1_e}^{NP} = 1$, $\eta^{NP} = 1$, $c_1^{AF} = 1$, $c_{1_e}^{AF} = 1$, $\eta^{AF} = 1$)

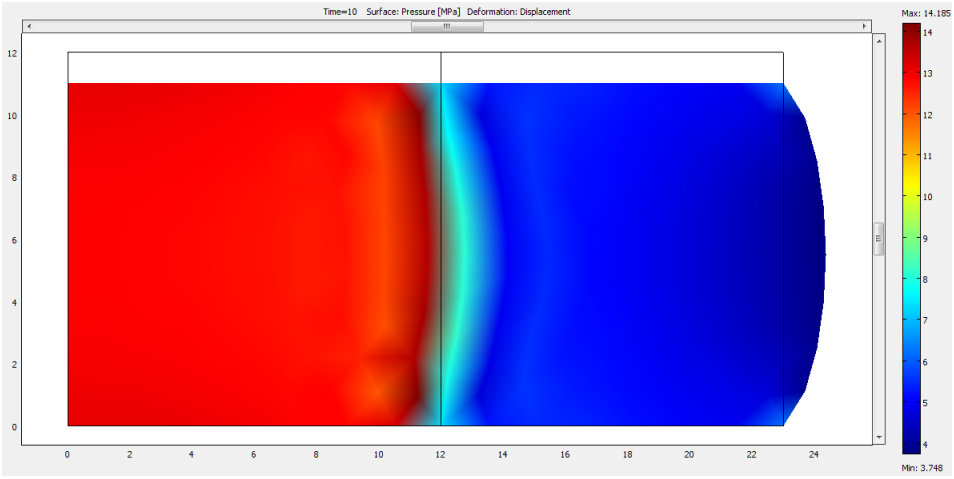

Figure 27: Pressure distribution within the IVD ($c_1^{NP} = 1$, $c_{1_e}^{NP} = 1$, $\eta^{NP} = 1$, $c_1^{AF} = 1$, $c_{1_e}^{AF} = 1$, $\eta^{AF} = 1$)

The map of the Von Mises stress distribution is displayed in Figure 28: the value of the stress on each element was not interpolated on this map, so that the interface between the NP and the AF can be easily localized. Higher stresses values characterize this interface, as well as the upper and lower extremities of the AF (remind that the nodes along the top and bottom of the model were constrained in r-direction to represent the attachment of the disc to the endplates and vertebral bodies, thus assumed infinitely rigid with respect to the IVD).

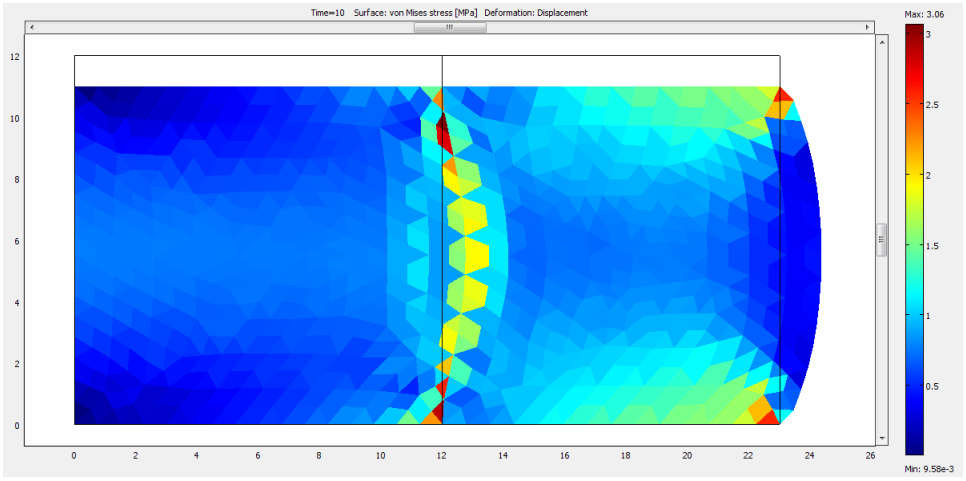

Figure 28: Von Mises stress distribution ($c_1^{NP} = 1$, $c_{1_e}^{NP} = 1$, $\eta^{NP} = 1$, $c_1^{AF} = 1$, $c_{1_e}^{AF} = 1$, $\eta^{AF} = 1$)

First set of simulations A first set of simulations was investigated. The loading characteristic time $\tau_{load} = 10$ s was chosen. The choice of a purely elastic material

was made for the AF and the NP was considered a viscoelastic Maxwell (fluid type) material, that results in the following values for the material constants (Table 3):

$c_{1_e}^{AF}$	η^{AF}	c_1^{AF}	c_1^{NP}
0.001	1	1	0.001

Table 3: Material constants fixed for the first set of simulations

Then, depending on the values of η^{NP} and $c_{1_e}^{NP}$, three series of three simulations were distinguished (Table 4). Series 1, Series 2 and Series 3 correspond to the cases $\tau^{NP} \gg \tau_{load}$, $\tau^{NP} \approx \tau_{load}$, and $\tau^{NP} \ll \tau_{load}$ respectively; whereas the associated letter a, b, c correspond to the cases $\tau_e^{NP} \approx \tau_{load}$, $\tau_e^{NP} \ll \tau_{load}$, and $\tau_e^{NP} \gg \tau_{load}$ respectively.

Series #	η^{NP}	τ^{NP}	$c_{1_e}^{NP}$	τ_e^{NP}	Simulation #
1	1	1000	0.1	10	1.a
			100	0.01	1.b
			0.001	1000	1.c
2	0.01	10	0.001	10	2.a
			1	0.01	2.b
			0.00001	1000	2.c
3	0.0001	0.1	0.00001	10	3.a
			0.01	0.01	3.b
			0.0000001	1000	3.c

Table 4: Series of simulations for the first set

The results of this first set of simulations are difficult to analyze. First, for the Series 1, simulations 1.a and 1.b did not converge for the material constants fixed in Table 3. The reasons why the calculation does not converge are not obvious. Figure 29 shows the force response (along z-direction) versus time for Series 2 and 3. From these curves, the response seems almost perfectly elastic whatever the choice of the viscoelastic parameters of the NP, and for the material constants fixed in Table 3. Thus, it would mean that the overall response is given by the response of the AF, and that the NP has no influence. The plot of the relative contributions of the AF and the NP to the overall force response (Figure 30) shows that the NP contributes to about 1/4 of the overall force response. That means that the behavior of the IVD is mainly governed by the AF contribution. However, it does not explain entirely the almost perfect elastic response which is observed.

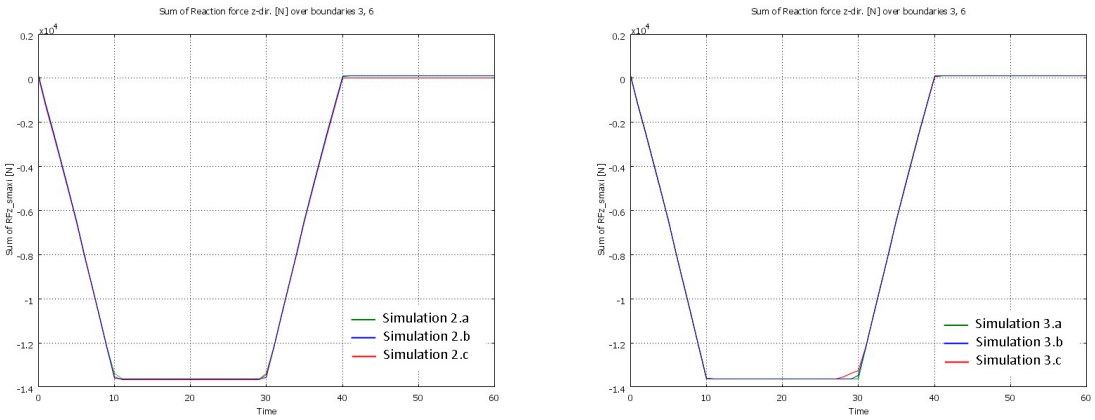

Figure 29: Force response (along z-direction) versus time for Series 2 (left) and 3 (right)

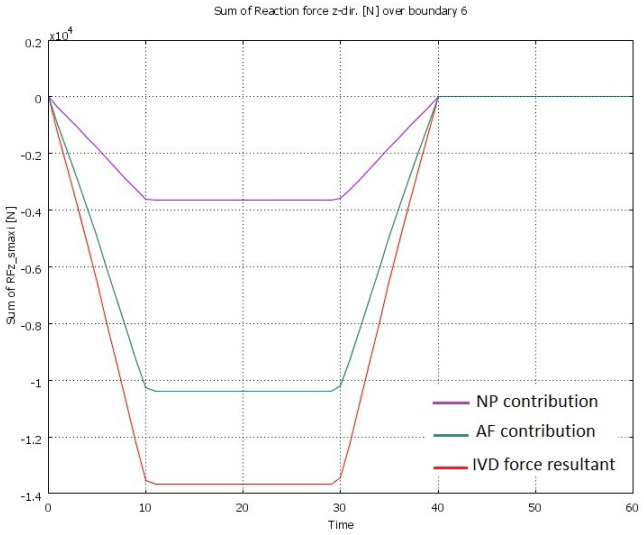

Figure 30: AF and NP relative contribution to the overall IVD resultant force for Simulation 2.b

Conclusion about the first set of simulations The conclusions that can derived from this first set of simulations are quite tricky. Indeed, for the material constants fixed in Table 3, the response for Series 2 and 3 are very similar, which does not correspond to what could have been expected. Since no viscous response of the NP is visible, one could first think that viscoelaticity was not correctly implemented within COMSOL. But, according to the validation process performed in Section 5.2, this explanation can be directly rejected. A second reason that could explain such results would be that the NP contribution is negligible when the IVD is loaded in compression, but this goes against the results found in the literature. It

is more likely that our model of the AF is too coarse: it does not take into account the fibrous structure of the AF which gives it a very different behavior whether it is loaded in traction or in compression.

On way to continue this work would be to run new sets of simulation (still varying the viscoelastic parameters η^{NP} and $c_{1_e}^{NP}$ as previously) with $c_1^{NP} = 0.01$ and $c_1^{NP} = 0.1$, keeping $c_1^{AF} = 1$ fixed. In that case, the ratio $\frac{c_1^{NP}}{c_1^{AF}}$ would increase and the difference of stiffness between NP and AF would be less important. However, those simulations could not be performed due to a lack of time.

6 Discussion

6.1 Summary

The IVD is a fibrocartilage that lies between bony vertebral bodies. It is comprised of the central gelatinous nucleus pulposus (NP) surrounded circumferentially by the annulus fibrosus (AF). The cartilaginous endplate forms an interface between the disc and adjacent vertebral bodies. The NP is structurally and mechanically isotropic and contains a network of collagen fibers interspersed with proteoglycans, resulting in a high water content within the tissue. The osmotic swelling that results is a defining feature of NP mechanics. Each lamella of the multi-lamellar AF consists of highly aligned collagen fibers whose orientation alternates above and below the transverse axis of the spine by approximately 30° in adjacent lamellae. This particular structure of the IVD offers to the spine high flexibility, and permits load transfer, and energy dissipation though the spine. However, due to aging and/or pathological state, disc degeneration may occur. This phenomenon is characterized by serious composition and structural changes within the IVD, thus entailing changes in the mechanical response and function of the IVD. Disc degeneration may often be associated to severe back pain.

Several analytic and finite element models have been used to predict the behavior of the IVD, to investigate the process of disc degeneration, or to understand the complex exchange mechanisms in the IVD. The present study, which was quite limited in time, focused on proposing a simple geometrical model of the IVD. The goal was to investigate its short-time mechanical response and the role of the NP and the AF when the IVD is subjected to simple loading (axial traction and compression). Since the overall behavior of the IVD show viscoelastic characteristic, non-linear (incompressible) viscoelasticity was chosen to model both the AF and the NP.

During this study, the theory of non-linear viscoelasticity was briefly described. Focus was made on its numerical implementation: the 1D analytical implementation was performed using Matlab, and the 3D and axisymmetric implementation was carried out using the finite element software COMSOL Multiphysics. The second implementation, which was quite tricky, was successfully validated against the analytical one.

The 1D analytical implementation was used to analyze the non-linear viscoelasticity constitutive law. Three material parameters were involved in this constitutive law (c_1, c_{1_e} , and η), thus defining two characteristic times: $\tau = \frac{\eta}{c_1}$ (the characteristic time to get the elastic response given by c_1), and $\tau_e = \frac{\eta}{c_{1_e}}$ (the time required to

get a purely viscous response in the viscoelastic branch.

Eventually, some simulations of the IVD behavior using non-linear incompressible viscoelasticity for both the AF and the NP were run. Due to a lack of time and convergence difficulties, a whole parameter analysis could not be performed. Only a few simulations were run, and the results found were proved to be quite unsatisfactory. Indeed, the overall behavior of the IVD showed no sign of viscoelastic effects when the viscoelastic part of the AF behaviour is set small, which was surprising considering the constitutive law which was used. The behavior of the disc seemed mainly governed by the elastic behavior of the AF. Decreasing the difference between the stiffness of the NP and the stiffness of the AF would maybe lead to a more viscoelastic response of the IVD. Whereas the simulations which were conducted here do not permit us to conclude whether the choice of non-linear viscoelasticity for the NP was relevant, it seems that the choice of the same constitutive law for the AF was not appropriate. Indeed, the anisotropy of the AF due to its highly oriented fibrous structure was not taken into account, while it must play an important role in the traction-compression response.

6.2 Open questions and future work

This work showed that it is possible to implement rich and rigorous rheological models from a mathematical point of view. But these models involve many parameters; consequently, the use of such models is difficult and the interpretation of the results may often be tricky. To face this problem and to be able to identify the effects which predominate in the AF and the NP, reliable experimental data are definitely required.

Then, in order to improve the analysis of the model, new simulations, where the difference of stiffness between AF and NP would be less important, should be performed. This would constitute a first step toward the comprehension of the viscoelastic parameters of the IVD components. Secondly, the anisotropy of the AF could be considered. In that purpose, one could rely on the theory of Holzapfel and Gasser [12]. The physics of the IVD could also be enriched in order to describe its long-term behavior: one could imagine a mechanical model coupled with diffusion for example.

References

[1] *COMSOL Multiphysics User's Guide.*

[2] Christopher D. Agosti. *Viscoelastic characterization of rabbit nucleus pulposus in torsional creep.* PhD thesis, University of Pittsburgh, 2006.

[3] M. Argoubi and A. Shirazi-Adl. Poroelastic creep response analysis of a lumbar motion segment in compression. *Journal of Biomechanics*, 29(10):1331 – 1339, 1996.

[4] G. Baroud, J. Nemes, P. Heini, and T. Steffen. Load shift of the intervertebral disc after a vertebroplasty: a finite-element study. *European Spine Journal*, 12:421–426, 2003.

[5] Amélie Burel. Numerical implementation of a non-linear constitutive equations for hydrogels. Master's thesis, 2009.

[6] Allen Carl, Eric Ledet, Hansen Yuan, and Alok Sharan. New developments in nucleus pulposus replacement technology. *The Spine Journal*, 4(6, Supplement 1):S325 – S329, 2004.

[7] Chen-Sheng Chen, Cheng-Kung Cheng, Chien-Lin Liu, and Wai-Hee Lo. Stress analysis of the disc adjacent to interbody fusion in lumbar spine. *Medical Engineering & Physics*, 23(7):485 – 493, 2001.

[8] W. Ehlers, N. Karajan, and B. Markert. An extended biphasic model for charged hydrated tissues with application to the intervertebral disc. *Biomechanics and Modeling in Mechanobiology*, 8:233–251, 2009.

[9] Alfonso Fantigrossi, Fabio Galbusera, Manuela Teresa Raimondi, Marco Sassi, and Maurizio Fornari. Biomechanical analysis of cages for posterior lumbar interbody fusion. *Medical Engineering & Physics*, 29(1):101 – 109, 2007.

[10] Stephen J. Ferguson, Keita Ito, and Lutz-P. Nolte. Fluid flow and convective transport of solutes within the intervertebral disc. *Journal of Biomechanics*, 37(2):213 – 221, 2004. Spinal Biomechanics.

[11] Maurice L. Goins, David W. Wimberley, Philip S. Yuan, Laurence N. Fitzhenry, and Alexander R. Vaccaro. Nucleus pulposus replacement: an emerging technology. *The Spine Journal*, 5(6, Supplement 1):S317 – S324, 2005.

[12] Gerhard A. Holzapfel and Thomas C. Gasser. A viscoelastic model for fiber-reinforced composites at finite strains: Continuum basis, computational aspects and applications. *Computer Methods in Applied Mechanics and Engineering*, 190(34):4379 – 4403, 2001.

[13] N. Huber and C. Tsakmakis. Finite deformation viscoelasticity laws. *Mechanics of Materials*, 32(1):1 – 18, 2000.

[14] David W. L. Hukins and Judith R. Meakin. Relationship between structure and mechanical function of the tissues of the intervertebral joint. *Amer. Zool.*, 40(1):42–52, 2000.

[15] James C. Iatridis, Lori A. Setton, Robert J. Foster, Bernard A. Rawlins, Mark Weidenbaum, and Van C. Mow. Degeneration affects the anisotropic and nonlinear behaviors of human anulus fibrosus in compression. *Journal of Biomechanics*, 31(6):535 – 544, 1998.

[16] Wade Johannessen, Edward J. Vresilovic, Alexander C. Wright, and Dawn M. Elliott. Intervertebral disc mechanics are restored following cyclic loading and unloaded recovery. *Annals of Biomedical Engineering*, 32:70–76, 2004.

[17] Alison C. Jones and Ruth K. Wilcox. Finite element analysis of the spine: Towards a framework of verification, validation and sensitivity analysis. *Medical Engineering & Physics*, 30(10):1287 – 1304, 2008. Special issue to commemorate the 30th anniversary of Medical Engineering & Physics - 30th Anniversary Issue.

[18] Stephen M. Klisch and Jeffrey C. Lotz. Application of a fiber-reinforced continuum theory to multiple deformations of the annulus fibrosus. *Journal of Biomechanics*, 32(10):1027 – 1036, 1999.

[19] D. S. McNally and R. G. C. Arridge. An analytical model of intervertebral disc mechanics. *Journal of Biomechanics*, 28(1):53 – 68, 1995.

[20] Judith R. Meakin and W. L. Hukins. Replacing the nucleus pulposus of the intervertebral disk: prediction of suitable properties of a replacement material using finite element analysis. *Journal of Materials Science: Materials in Medicine*, 12:207–213, 2001.

[21] Judith R. Meakin, Janet E. Reid, and David W. L. Hukins. Replacing the nucleus pulposus of the intervertebral disc. *Clinical Biomechanics*, 16(7):560 – 565, 2001.

[22] Antonius Rohlmann, Thomas Zander, Hendrik Schmidt, Hans-Joachim Wilke, and Georg Bergmann. Analysis of the influence of disc degeneration on the mechanical behaviour of a lumbar motion segment using the finite element method. *Journal of Biomechanics*, 39(13):2484 – 2490, 2006.

[23] Yvonne Schroeder, Wouter Wilson, Jacques M. Huyghe, and Frank P. T. Baaijens. Osmoviscoelastic finite element model of the intervertebral disc. *European spine journal*, 15:S361–S371, 2006.

[24] Hariharan Shankar, Jeremy A. Scarlett, and Stephen E. Abram. Anatomy and pathophysiology of intervertebral disc disease. *Techniques in Regional Anesthesia and Pain Management*, 13(2):67 – 75, 2009. Discogenic Back Pain: Converging Data, Hypotheses, and Techniques.

[25] B. R. Simon, J. S. S. Wu, M. W. Carlton, J. H. Evans, and L. E. Kazarian. Structural models for human spinal motion segments based on a poroelastic view of the intervertebral disk. *Journal of Biomechanical Engineering*, 107(4):327–335, 1985.

[26] Jill P.G. Urban and Sally Roberts. Development and degeneration of the intervertebral discs. *Molecular Medicine Today*, 1(7):329 – 335, 1995.

[27] Jun Yao, Sergio R Turteltaub, and Paul Ducheyne. A three-dimensional nonlinear finite element analysis of the mechanical behavior of tissue engineered intervertebral discs under complex loads. *Biomaterials*, 27(3):377 – 387, 2006. Biomaterials for Spinal Applications, Biomaterials for Spinal Applications.

7 Appendix

A Euler method applied to the deformation gradient tensor

At time t, all variables are known. If $\mathbf{F}$ is the deformation gradient tensor, from calculus we know that we can write at time $t + \Delta t$:

$$\dot{\mathbf{F}}\left(t + \Delta t\right) = \frac{\mathbf{F}\left(t + \Delta t\right) - \mathbf{F}\left(t\right)}{\Delta t} \tag{1}$$

provided Δt is small enough. $\mathbf{F}$ is related to the Eulerian velocity gradient $\mathbf{L}$ through $\mathbf{L} = \dot{\mathbf{F}}\mathbf{F}^{-1}$ or equivalently

$$\dot{\mathbf{F}}\left(t + \Delta t\right) = \mathbf{L}\left(t + \Delta t\right)\mathbf{F}\left(t + \Delta t\right). \tag{2}$$

Using Eq. (1), the previous equation becomes

$$\mathbf{F}\left(t + \Delta t\right) = \mathbf{F}\left(t\right) + \Delta t \cdot \mathbf{L}\left(t + \Delta t\right)\mathbf{F}\left(t + \Delta t\right) \tag{3}$$

or equivalently after rearranging

$$\mathbf{F}\left(t + \Delta t\right) = \left[\mathbf{I} - \Delta t \cdot \mathbf{L}\left(t + \Delta t\right)\right]^{-1}\mathbf{F}\left(t\right) \tag{4}$$

where $\mathbf{I}$ is the identity tensor. In some particular cases, including uniaxial extension, $\mathbf{L}$ and its symmetric part $\mathbf{D}$ (Eulerian strain rate tensor) coincide. Thus, we can write

$$\mathbf{F}\left(t + \Delta t\right) = \left[\mathbf{I} - \Delta t \cdot \mathbf{D}\left(t + \Delta t\right)\right]^{-1}\mathbf{F}\left(t\right). \tag{5}$$

The above equation is still valid even if we replace $\mathbf{F}$ and $\mathbf{D}$ by $\mathbf{F}_v$ and $\mathbf{D}_v$ respectively.

B Matlab program of the 1D analytical model

```
%=========================================================================================%
%                                                                                         %
%          STRESS CALCULATION ALGORITHM FOR FINITE STRAIN VISCOELASTICITY                 %
%                    USING THE NEO-HOOKE HYPERELASTIC MODEL                               %
%                                                                                         %
%=========================================================================================%


% The goal of this programme is to compute the stress response of a
% visco-hyperelastic rheological model (spring A // (spring B + dashpot B))
% in large deformations (finite strain) submitted to an uniaxial traction
% test.
%
% For the whole model, the deformation is the same in network A and network
% B, that means
%       F = FA = FB.
% Moreover, the deformation in network B can be decomposed into an elastic
% part and an inelastix part:
%       FB = Fe*Fi.
%
% A hyperelastic neo-Hooke law is used for the springs :
%       WA = C1*(IB1-3) and WB = C1e*(IBe1-3)
% Thus, we have:
%        sigmaA = -pA*I + 2*(dWA/dB)*B = -pA*I + 2*(dWA/dI1B)*B = -pA*I + 2*C1*B,
%        sigmaB = -pB*I + 2*(dWB/dBe)*Be = -pB*I + 2*(dWB/dI1Be)*Be = -pB*I + 2*C1e*Be,
% and
%       sigma = sigmaA + sigmaB.


clear all;
clc;
close all;


%=========================================================================================%
%                                      INITIAL STEP                                       %
%=========================================================================================%


% INPUT

% Triangular signal
moy = 1;
ampli = 0.5;
alpha = 0.05;

b1 = moy;
t1 = ampli/alpha;
b2 = moy + 2*ampli;
t2 = 3*t1;
tfinal = 2*t1;
dt = t1/1000;

% Material constants
```

```
C1 = 1;
KK = 1;
C1e = 0.1;
eta = 1;

% Error
errorlimit = 1e-6;

% Identity tensor
I = eye(3,3);


%=========================================================================================%
%                   INITIAL VALUES OF VARIABLES (t=0)                                     %
%=========================================================================================%


t = 0;

% Initial deformation tensor
F0 = I;
% Initial inelastic (viscous) deformation tensor
Fi0 = I;
% Initial rate of viscous deformation tensor
Di0 = zeros(3,3);


%=========================================================================================%
%                  LOOPING FOR VARIABLES VALUES (at instant "t+dt")                       %
%=========================================================================================%


% PRE-LOOPING
Fi2 = inv(I-(dt*Di0))*Fi0;
Fi = Fi2;
Fi3 = Fi;
lambdai = Fi2(1,1);

% MAIN LOOPING

t = t+dt;
j = 1;

while t<tfinal

    % lambda is imposed
    % Triangular imput
    if t<t1
        lambda = b1+alpha*t;
    elseif t<t2
        lambda = b2-alpha*t;
    end

    % Sinusoidal input
    %lambda = 1 + 0.5*sin(pi*t/20);
    %lambda = moy + 0.5*sin(pi*t*alpha);
```

```
    % Network A (equilibrium network)
    F = [lambda 0 0 ; 0 1/(lambda^0.5) 0 ; 0 0 1/(lambda^0.5)];     % Deformation↙
tensor
    B = F*transpose(F);                     % Left Cauchy-Green stress tensor
    IB1 = trace(B);                         % 1st invariant of the left Cauchy-Green↙
stress tensor
    pA = 2*C1*B(3,3);
    SigmaA = -pA*I + 2*C1*B;     % Cauchy stress tensor

    % Network B (time-dependant network)
    if KK > 0
        error = 1;
        compteur = 0;

        while error > errorlimit

            % Computation of the elastic deformation tensor, depending on
            % the previous value of the inelastic part
            lambdae = lambda/lambdai;
            Fe = [lambdae 0 0 ; 0 lambdae^(-0.5) 0 ; 0 0 lambdae^(-0.5)];       %↙
Elastic deformation tensor
            Be = Fe*transpose(Fe);          % Elastic left Cauchy-Green stress tensor
            Ce = transpose(Fe)*Fe;          % Elastic right Cauchy-Green stress tensor
            IBe1 = trace(Be);               % Remark: IBe1 = trace(Ce) also
            pB = 2*C1e*Be(3,3);
            SigmaB = -pB*I + 2*C1e*Be;      % Elastic Cauchy stress tensor

            % Error on the inelastic part
            Di = 2*C1e/eta*(Ce-1/3*IBe1*I);
            Fi2 = inv(I-(dt*Di))*Fi;
            lambdai = Fi2(1,1);
            lambdai_prec = Fi3(1,1);
            error = abs(lambdai - lambdai_prec);
            Fi3 = Fi2;

            compteur = compteur+1;
        end

        Fi = Fi2;

    else
        SigmaB = 0;

    end

    %Total Cauchy stress tensor
    Sigmatotal = SigmaA + SigmaB;

    %PK1 stress tensor
    PK1total = Sigmatotal*inv(transpose(F));

    %Results
    Matlambda(j) = lambda;
    MatT(j) = t;
    MatSt1(j) = Sigmatotal(1,1);
```

```
    %MatPK1tot(j) = PK1total(1,1);
    MatF1(j) = F(1,1);

    j = j + 1;
    t = t + dt;

end

% RESULTS

% Plot of the input signal
figure(1);
plot(MatT, Matlambda, '-b', 'LineWidth', 2);
title('Stretch ratio versus time', 'FontSize', 12);
xlabel('t', 'FontSize', 12);
ylabel('\lambda', 'FontSize', 12);
grid on;

% Plot of the stress in the traction direction
figure(2);
plot(MatF1, MatSt1, '-k', 'LineWidth', 2);
title('Stress versus stretch in the traction direction', 'FontSize', 12);
xlabel('\lambda_1_1','FontSize',12);
ylabel('\sigma_1_1', 'FontSize', 12);
grid on;
hold on;

% Plot of the stress in the traction direction
figure(3);
plot(MatT, MatSt1, '-k', 'LineWidth', 2);
title('Axial stress versus time', 'FontSize', 12);
xlabel('t','FontSize',12);
ylabel('\sigma_1_1', 'FontSize', 12);
grid on;
hold on;
```

C COMSOL models implementation, expressions settings

Table of scalar expressions for the 3D model

Name	Expression	Description
F11_t	uxt	Time derivative of the deformation gradient 11 comp.
F12_t	uyt	Time derivative of the deformation gradient 12 comp.
F13_t	uzt	Time derivative of the deformation gradient 13 comp
F21_t	vxt	Time derivative of the deformation gradient 21 comp.
F22_t	vyt	Time derivative of the deformation gradient 22 comp.
F23_t	vzt	Time derivative of the deformation gradient 23 comp.
F31_t	wxt	Time derivative of the deformation gradient 31 comp.
F32_t	wyt	Time derivative of the deformation gradient 32 comp.
F33_t	wzt	Time derivative of the deformation gradient 33 comp.
Lxx_1	F11_t*invF11_smsld + F12_t*invF21_smsld + F13_t*invF31_smsld	Spatial velocity gradient tensor xx comp.
Lxy_1	F11_t*invF12_smsld + F12_t*invF22_smsld + F13_t*invF32_smsld	Spatial velocity gradient tensor xy comp.
Lxz_1	F11_t*invF13_smsld + F12_t*invF23_smsld + F13_t*invF33_smsld	Spatial velocity gradient tensor xz comp.
Lyx_1	F21_t*invF11_smsld + F22_t*invF21_smsld + F23_t*invF31_smsld	Spatial velocity gradient tensor yx comp.

Lyy_1	F21_t*invF12_smsld + F22_t*invF22_smsld + F23_t*invF32_smsld	Spatial velocity gradient tensor yy comp.
Lyz_1	F21_t*invF13_smsld + F22_t*invF23_smsld + F23_t*invF33_smsld	Spatial velocity gradient tensor yz comp.
Lzx_1	F31_t*invF11_smsld + F32_t*invF21_smsld + F33_t*invF31_smsld	Spatial velocity gradient tensor zx comp.
Lzy_1	F31_t*invF12_smsld + F32_t*invF22_smsld + F33_t*invF32_smsld	Spatial velocity gradient tensor zy comp.
Lzz_1	F31_t*invF13_smsld + F32_t*invF23_smsld + F33_t*invF33_smsld	Spatial velocity gradient tensor zz comp.
traceBe	Bexx_1 + Beyy_1 + Bezz_1	Trace of the elastic left Cauchy-Green strain tensor
devBexx_1	Bexx_1 - 1/3*traceBe*1	Deviatoric of the elastic left Cauchy-Green strain tensor xx comp.
devBexy_1	Bexy_1	Deviatoric of the elastic left Cauchy-Green strain tensor xy comp.
devBexz_1	Bexz_1	Deviatoric of the elastic left Cauchy-Green strain tensor xz comp.
devBeyx_1	Beyx_1	Deviatoric of the elastic left Cauchy-Green strain tensor yx comp.
devBeyy_1	Beyy_1 - 1/3*traceBe*1	Deviatoric of the elastic left Cauchy-Green strain tensor yy comp.
devBeyz_1	Beyz_1	Deviatoric of the elastic left Cauchy-Green strain tensor yz comp.

devBezx_1	Bezx_1	Deviatoric of the elastic left Cauchy-Green strain tensor zx comp.
devBezy_1	Bezy_1	Deviatoric of the elastic left Cauchy-Green strain tensor zy comp.
devBezz_1	Bezz_1 - 1/3*traceBe*1	Deviatoric of the elastic left Cauchy-Green strain tensor zz comp.
sourcexx_1	Bexx_1*Lxx_1 + Bexy_1*Lxy_1 + Bexz_1*Lxz_1 + Lxx_1*Bexx_1 + Lxy_1*Beyx_1 + Lxz_1*Bezx_1 - 4*C1e/eta*(Bexx_1*devBexx_1 + Bexy_1*devBeyx_1 + Bexz_1*devBezx_1)	Source term xx comp.

sourcexy_1	Bexx_1*Lyx_1 + Bexy_1*Lyy_1 + Bexz_1*Lyz_1 + Lxx_1*Bexy_1 + Lxy_1*Beyy_1 + Lxz_1*Bezy_1 - 4*C1e/eta*(Bexx_1*devBexy_1 + Bexy_1*devBeyy_1 + Bexz_1*devBezy_1)	Source term xy comp.
sourcexz_1	Bexx_1*Lzx_1 + Bexy_1*Lzy_1 + Bexz_1*Lzz_1+Lxx_1*Bexz_1 + Lxy_1*Beyz_1+Lxz_1*Bezz_1 - 4*C1e/eta* (Bexx_1*devBexz_1 + Bexy_1*devBeyz_1 + Bexz_1*devBezz_1)	Source term xz comp.
sourceyx_1	Beyx_1*Lxx_1 + Beyy_1*Lxy_1 + Beyz_1*Lxz_1 + Lyx_1*Bexx_1 + Lyy_1*Beyx_1 + Lyz_1*Bezx_1 - 4*C1e/eta*(Beyx_1*devBexx_1 + Beyy_1*devBeyx_1 + Beyz_1*devBezx_1)	Source term yx comp.

sourceyy_1	Beyx_1*Lyx_1 + Beyy_1*Lyy_1 + Beyz_1*Lyz_1 + Lyx_1*Bexy_1 + Lyy_1*Beyy_1 + Lyz_1*Bezy_1 - 4*C1e/eta*(Beyx_1*devBexy_1 + Beyy_1*devBeyy_1 + Beyz_1*devBezy_1)	Source term yy comp.
sourceyz_1	Beyx_1*Lzx_1 + Beyy_1*Lzy_1 + Beyz_1*Lzz_1 + Lyx_1*Bexz_1 + Lyy_1*Beyz_1 + Lyz_1*Bezz_1 - 4*C1e/eta*(Beyx_1*devBexz_1 + Beyy_1*devBeyz_1 + Beyz_1*devBezz_1)	Source term yz comp.
sourcezx_1	Bezx_1*Lxx_1 + Bezy_1*Lxy_1 + Bezz_1*Lxz_1 + Lzx_1*Bexx_1 + Lzy_1*Beyx_1 + Lzz_1*Bezx_1 - 4*C1e/eta*(Bezx_1*devBexx_1 + Bezy_1*devBeyx_1 + Bezz_1*devBezx_1)	Source term zx comp.

sourcezy_1	Bezx_1*Lyx_1 + Bezy_1*Lyy_1 + Bezz_1*Lyz_1 + Lzx_1*Bexy_1 + Lzy_1*Beyy_1 + Lzz_1*Bezy_1 - 4*C1e/eta*(Bezx_1*devBexy_1 + Bezy_1*devBeyy_1 + Bezz_1*devBezy_1)	Source term zy comp.
sourcezz_1	Bezx_1*Lzx_1 + Bezy_1*Lzy_1 + Bezz_1*Lzz_1 + Lzx_1*Bexz_1 + Lzy_1*Beyz_1 + Lzz_1*Bezz_1 - 4*C1e/eta*(Bezx_1*devBexz_1 + Bezy_1*devBeyz_1 + Bezz_1*devBezz_1)	Source term zz comp.
PK1xx_1	-p*invF11_smsld + 2*C1*F11_smsld + 2*C1e*(Bexx_1*invF11_smsld + Bexy_1*invF12_smsld + Bexz_1*invF13_smsld)	First Piola-Kirchhoff stress tensor xx comp.
PK1xy_1	-p*invF21_smsld + 2*C1*F12_smsld + 2*C1e*(Bexx_1*invF21_smsld + Bexy_1*invF22_smsld + Bexz_1*invF23_smsld)	First Piola-Kirchhoff stress tensor xy comp.
PK1xz_1	-p*invF31_smsld + 2*C1*F13_smsld + 2*C1e*(Bexx_1*invF31_smsld + Bexy_1*invF32_smsld + Bexz_1*invF33_smsld)	First Piola-Kirchhoff stress tensor xz comp.

PK1yx_1	-p*invF12_smsld + 2*C1*F21_smsld + 2*C1e*(Beyx_1*invF11_smsld + Beyy_1*invF12_smsld + Beyz_1*invF13_smsld)	First Piola-Kirchhoff stress tensor yx comp.
PK1yy_1	-p*invF22_smsld + 2*C1*F22_smsld + 2*C1e*(Beyx_1*invF21_smsld + Beyy_1*invF22_smsld + Beyz_1*invF23_smsld)	First Piola-Kirchhoff stress tensor yy comp.
PK1yz_1	-p*invF32_smsld + 2*C1*F23_smsld + 2*C1e*(Beyx_1*invF31_smsld + Beyy_1*invF32_smsld + Beyz_1*invF33_smsld)	First Piola-Kirchhoff stress tensor yz comp.
PK1zx_1	-p*invF13_smsld + 2*C1*F31_smsld + 2*C1e*(Bezx_1*invF11_smsld + Bezy_1*invF12_smsld + Bezz_1*invF13_smsld)	First Piola-Kirchhoff stress tensor zx comp.
PK1zy_1	-p*invF23_smsld + 2*C1*F32_smsld + 2*C1e*(Bezx_1*invF21_smsld + Bezy_1*invF22_smsld + Bezz_1*invF23_smsld)	First Piola-Kirchhoff stress tensor zy comp.
PK1zz_1	-p*invF33_smsld + 2*C1*F33_smsld + 2*C1e*(Bezx_1*invF31_smsld + Bezy_1*invF32_smsld + Bezz_1*invF33_smsld)	First Piola-Kirchhoff stress tensor zz comp.

Table of scalar expressions for the axisymmetric model

Name	Expression	Description
Frr_t	uorrt*r + uort	Time derivative of the deformation gradient rr comp.

Frz_t	uorzt*r	Time derivative of the deformation gradient rz comp.
F22_t	uort	Time derivative of the deformation gradient 22 comp.
Fzr_t	wrt	Time derivative of the deformation gradient zr comp.
Fzz_t	wzt	Time derivative of the deformation gradient zz comp.
Lrr_1	Frr_t*invF11_smaxi + Frz_t*invF31_smaxi	Spatial velocity gradient tensor rr comp.
Lrz_1	Frr_t*invF13_smaxi + Frz_t*invF33_smaxi	Spatial velocity gradient tensor rz comp.
L22_1	F22_t*invF22_smaxi	Spatial velocity gradient tensor 22 comp.
Lzr_1	Fzr_t*invF11_smaxi + Fzz_t*invF31_smaxi	Spatial velocity gradient tensor zr comp.
Lzz_1	Fzr_t*invF13_smaxi + Fzz_t*invF33_smaxi	Spatial velocity gradient tensor zz comp.
traceBe	Berr_1 + Be22_1 + Bezz_1	Trace of the elastic left Cauchy-Green strain tensor
devBerr_1	Berr_1 - 1/3*traceBe*1	Deviatoric of the elastic left Cauchy-Green strain tensor rr comp.
devBerz_1	Berz_1	Deviatoric of the elastic left Cauchy-Green strain tensor rz comp.
devBe22_1	Be22_1 - 1/3*traceBe*1	Deviatoric of the elastic left Cauchy-Green strain tensor 22 comp.
devBezr_1	Bezr_1	Deviatoric of the elastic left Cauchy-Green strain tensor zr comp.
devBezz_1	Bezz_1 - 1/3*traceBe*1	Deviatoric of the elastic left Cauchy-Green strain tensor zz comp.

sourcerr_1	Berr_1*Lrr_1 + Berz_1*Lrz_1 + Lrr_1*Berr_1 + Lrz_1*Bezr_1 - 4*C1e/eta*(Berr_1*devBerr_1 + Berz_1*devBezr_1)	Source term rr comp.
sourcerz_1	Berr_1*Lzr_1 + Berz_1*Lzz_1 + Lrr_1*Berz_1 + Lrz_1*Bezz_1 - 4*C1e/eta*(Berr_1*devBerz_1 + Berz_1*devBezz_1)	Source term rz comp.
source22_1	Be22_1*L22_1 + L22_1*Be22_1 - 4*C1e/eta*Be22_1*devBe22_1	Source term 22 comp.
sourcezr_1	Bezr_1*Lrr_1 + Bezz_1*Lrz_1 + Lzr_1*Berr_1 + Lzz_1*Bezr_1 - 4*C1e/eta*(Bezr_1*devBerr_1 + Bezz_1*devBezr_1)	Source term zr comp.
sourcezz_1	Bezr_1*Lzr_1 + Bezz_1*Lzz_1 + Lzr_1*Berz_1 + Lzz_1*Bezz_1 - 4*C1e/eta*(Bezr_1*devBerz_1 + Bezz_1*devBezz_1)	Source term zz comp.
PK1rr_1	-p*invF11_smaxi + 2*C1*F11_smaxi + 2*C1e*(Berr_1*invF11_smaxi + Berz_1*invF13_smaxi)	First Piola-Kirchhoff stress tensor rr comp.
PK1rz_1	-p*invF31_smaxi + 2*C1*F13_smaxi + 2*C1e*(Berr_1*invF31_smaxi + Berz_1*invF33_smaxi)	First Piola-Kirchhoff stress tensor rz comp.
PK122_1	-p*invF22_smaxi + 2*C1*F22_smaxi + 2*C1e*Be22_1*invF22_smaxi	First Piola-Kirchhoff stress tensor 22 comp.
PK1zr_1	-p*invF13_smaxi + 2*C1*F31_smaxi + 2*C1e*(Bezr_1*invF11_smaxi + Bezz_1*invF13_smaxi)	First Piola-Kirchhoff stress tensor zr comp.

PK1zz_1	-p*invF33_smaxi + 2*C1*F33_smaxi + 2*C1e*(Bezr_1*invF31_smaxi + Bezz_1*invF33_smaxi)	First Piola-Kirchhoff stress tensor zz comp.